Deep ocean circulation and transport where the East Pacific Rise at 9–10°N meets the Lamont seamount chain

J. W. Lavelle,[1] A. M. Thurnherr,[2] J. R. Ledwell,[3] D. J. McGillicuddy Jr.,[3] and L. S. Mullineaux[4]

Received 25 May 2010; revised 3 September 2010; accepted 4 October 2010; published 31 December 2010.

[1] We report the first 3-D numerical model study of abyssal ocean circulation and transport over the steep topography of the East Pacific Rise (EPR) and adjoining Lamont seamount chain in the eastern tropical Pacific. We begin by comparing results of hydrodynamical model calculations with observations of currents, hydrography, and SF_6 tracer dispersion taken during Larval Dispersal on the Deep East Pacific Rise (LADDER) field expeditions in 2006–2007. Model results are then used to extend observations in time and space. Regional patterns are pronounced in their temporal variability at M_2 tidal and subinertial periods. Mean velocities show ridge-trapped current jets flowing poleward west and equatorward east of the ridge, with time-varying magnitudes (weekly average maximum of ~10 cm s^{-1}) that make the jets important features with regard to ridge-originating particle/larval transport. Isotherms bow upward over the ridge and plunge downward into seamount flanks below ridge crest depth. The passage (P1) between the EPR and the first Lamont seamount to the west is a choke point for northward flux at ridge crest depths and below. Weekly averaged velocities show times of anticyclonic flow around the Lamont seamount chain as a whole and anticyclonic flow around individual seamounts. Results show that during the LADDER tracer experiment SF_6 reached P1 from the south in the western flank jet. A short-lived change in regional flow direction, just at the time of SF_6 arrival at P1, started the transport of SF_6 to the west on a course south of the seamounts, as field observations suggest. Approximately 20 days later, a longer-lasting shift in regional flow from west to SSE returned a small fraction of the tracer to the EPR ridge crest.

Citation: Lavelle, J. W., A. M. Thurnherr, J. R. Ledwell, D. J. McGillicuddy Jr., and L. S. Mullineaux (2010), Deep ocean circulation and transport where the East Pacific Rise at 9–10°N meets the Lamont seamount chain, *J. Geophys. Res.*, *115*, C12073, doi:10.1029/2010JC006426.

1. Introduction

[2] In years 2006–2007, the Larval Dispersal on the Deep East Pacific Rise (LADDER) project group conducted biological field experiments [e.g., *Mullineaux et al.*, 2010] and measured the physical environment along the northern half of the East Pacific Rise (EPR) segment lying between 9° and 10°N. The overall goal of the project has been to advance the understanding of the transport of biological materials between hydrothermal vent fields along the ridge. As part of that effort, a 3-D hydrodynamical model was employed to provide a framework for the physical oceanographic measurements [*Jackson et al.*, 2010; A. M. Thurnherr et al., Circulation near the crest of the East Pacific Rise between 9° and 10°N, submitted to *Deep Sea Research*, 2010] and to provide a backbone for larval transport calculations of the kind begun by *McGillicuddy et al.* [2010]. A separate modeling goal has been to gain a better understanding, both descriptive and dynamical, of the influences of abrupt topography on deep flow. The present paper focuses on the 3-D modeling of flow and transport over the initial 2 month period of LADDER, a time period over which physical oceanographic measurements were most intensive and during which an SF_6 tracer dispersion experiment was conducted [*Jackson et al.*, 2010]. We describe the model configuration, show comparisons with LADDER field measurements during that time period, and then use the model to extrapolate circulation and transport patterns in the deep ocean over a domain encompassing the northern half of this EPR segment. This descriptive account documents the strong variability in space and time of flow and transport in this region. A

[1] NOAA Pacific Marine Environmental Laboratory, Seattle, Washington, USA.
[2] Division of Ocean and Climate Physics, Lamont-Doherty Earth Observatory, Palisades, New York, USA.
[3] Department of Applied Ocean Physics and Engineering, Woods Hole Oceanographic Institution, Woods Hole, Massachusetts, USA.
[4] Department of Biology, Woods Hole Oceanographic Institution, Woods Hole, Massachusetts, USA.

0148-0227/10/2010JC006426

discussion of the dynamics underlying important features of these fields is left for a subsequent paper.

[3] Direct and indirect measurements of deep circulation at the 9–10°N segment suggest that mean flow is westward [*Baker et al.*, 1994] at speeds of ~0.5 cm s^{-1} [*Marsh et al.*, 2001; Thurnherr et al., submitted manuscript, 2010]. Data from current meters moored within 200 m of the seafloor above the shallow axial trough of the ridge crest [e.g., *Marsh et al.*, 2001] showed that semidiurnal tidal and low-frequency (T > 200 h) motions contain two thirds of the kinetic energy of motion above the ridge. Long-period flow directly above the ridge crest exhibits a tendency to have a larger along-ridge (~meridional) than across-ridge (~zonal) component [*Marsh et al.*, 2001; *Adams and Mullineaux*, 2008; Thurnherr et al., submitted manuscript, 2010] as had been seen at 13°N on the EPR by *Chevaldonné et al.* [1997]. Long-term mean flows measured on the flanks within a few tens of kilometers of the crest are poleward to the west [*Adams*, 2007; Thurnherr et al., submitted manuscript, 2010] and equatorward to the east (Thurnherr et al., submitted manuscript, 2010) of the ridge. Anticyclonically sheared mean flow of a similar nature had been observed, but only above ridge crest depth, on the Cleft segment of Juan de Fuca Ridge (JdFR) [*Cannon et al.*, 1991; *Cannon and Pashinski*, 1997; *Helfrich et al.*, 1998]. Currents have also been examined in and above the axial valley at the Mid-Atlantic Ridge [e.g., *Keller et al.*, 1975; *Thurnherr et al.*, 2008] and on the Endeavor segment of the JdFR [e.g., *Thomson et al.*, 2003; *Berdeal et al.*, 2006; *Thomson et al.*, 2009], but those locales have deep-walled axial valleys making the ridge crest bathymetry unlike that of EPR 9–10°N [*Fornari et al.*, 1998].

[4] Measurements of hydrography over ridge crests can be found at two levels of resolution. Hydrographic transects spanning ocean basins often show isotherms bending downward into both sides of a ridge [e.g., *Stommel et al.*, 1973; *Joyce*, 1981; *Wunsch et al.*, 1983; *Thompson and Johnson*, 1996]. At a finer horizontal resolution (5–10 km), hydrographic sections are more complex. Doming of isotherms/isopycnals directly over ridge crests is often found [*Cannon et al.*, 1991; *Cannon and Pashinski*, 1997; Thurnherr et al., submitted manuscript, 2010] as is plunging of isotherms/isopycnals into the ridge flanks, though not necessarily on both sides. (The word flank will be used here to designate a side of the ridge to a distance of a few tens of kilometers.) In some cases, the across-ridge distribution of isopycnals can be asymmetric, with uplifted isopycnals on one side and downset isopycnals of the other side. In other cases, however, isopycnals plunge directly into the ridge crest rather than dome above it [*Crane et al.*, 1985; *Helfrich et al.*, 1998]. Those transects have been interpreted to be showing effects of hydrothermal heat vented at the ridge crest.

[5] The model description offered here should be expected to contain the general features just described, save for dipping isopycnals into the ridge crest. The reason for the exception is that buoyancy forcing stemming from hydrothermal venting is not considered in this model. Effects on hydrography, at ridge crests without deep axial valleys, should be observable on transects passing directly over a discharge site but not on transects a few hundred meters up or down ridge. Particle concentration rather than temperature is thus typically used to follow hydrothermal plumes off axis and away from vent fields [e.g., *Baker et al.*, 1994].

[6] Along the EPR, hydrothermal discharge tends to occur in small patches (vent fields, ~1000 m^2) typically widely spaced (~10–50 km) along the ridge crest [*Haymon et al.*, 1991]. Thus only a very small fraction of the EPR ridge length is hydrothermally active. Moreover, effects of hydrothermal discharge on flow generally occur only at small space scales. Using a 3-D nonhydrostatic model, *Lavelle* [1997] showed that velocities of measurable size occur at distances of at most a few 100s of meters horizontally around typical hydrothermal vent fields. A counterexample is that of hydrothermal discharge occurring in a topographically confined region. *Thomson et al.* [2009] modeled the effects of the buoyancy flux from five closely spaced vent fields at Endeavor Ridge in the northeast Pacific, where venting occurs at the bottom of a steep walled, 100–200 m deep, axial valley. Their model suggests that hydrothermal discharge causes a mean along-valley flow over a length scale much larger than that of a single vent field. The bathymetry of the deep axial valley at the crest of Endeavor Ridge, however, is much different than the shallow trough at the crest of the EPR [*Fornari et al.*, 1988]. Little topographic channelization of flow can be expected in the second locale. Since flow and hydrographic effects of hydrothermal venting at the EPR will occur locally and at isolated sites and at length scales too small to be resolved in our model, we chose not to include buoyancy from hydrothermal discharge in model forcing.

[7] Furthermore, the model is focused on abyssal flow and transport, so no representation is implied that the model accurately describes conditions in the upper ocean. Attempting to directly connect the conditions in the upper ocean, i.e., surface wind, atmospheric pressure, heating, precipitation, or the occasional transit of apparently shallow Papaguyo and Tehuantepec eddies [e.g., *Fiedler and Talley*, 2006; *Adams and Flierl*, 2010] across the region to motion at this deep ridge is well beyond what we intend to do. Instead, we seek to replicate as faithfully as possible features of the deep ocean current, hydrography, and tracer observations for the first two months of the LADDER period and then use the model to draw a larger, more-detailed picture of deep ocean conditions in this region. Model results are used to study the time variation of rectified flow along ridge flanks, patterns of isopycnal doming over the ridge in relation to background currents, the variability of fluid flux though the passage between ridge and seamounts, the pathway of the SF_6 between the time of release and first measurement in the field experiment, and the flow patterns that caused SF_6 to be transported primarily westward on a trajectory south of the seamounts rather than northward to the ridge tip.

[8] This numerical ocean model differs from many others in that the focus is on abyssal flow and transport; the domain is regional in scope and thus has four open boundaries; the need to simulate actual SF_6 dispersion requires multi-frequency forcing consistent with observed currents; and the length of the tracer experiment mandates efficient suppression of internal wave reflection at domain boundaries. The need to match field and model currents is most intense just subsequent to the time of tracer injection. A misdirected current at that time could advect model tracer to the wrong side of the ridge and into a quite different flow pattern, never to regain the path of the observed tracer. To solve this problem, model forcing is derived from currents observed

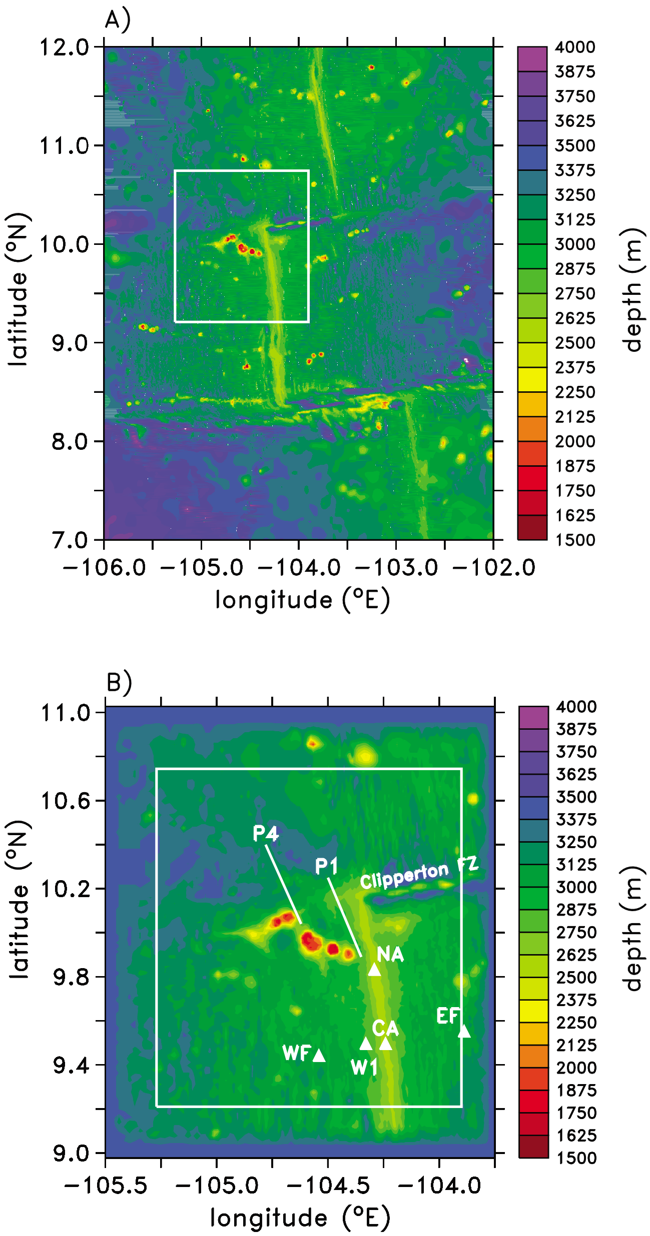

Figure 1. (a) Bathymetry of the East Pacific Rise between 7 and 12°N. The 9–10°N segment is offset to the west of adjoining segments by the Clipperton Fracture Zone at ~10.25°N and the Sequeiros Fracture Zone at ~8.4°N. The modeling work here is focused on the region outlined in white. Gridded bathymetry is from the Lamont-Doherty Earth Observatory archives. (b) The model domain is bounded by coordinates 9–11°N and 105.5–103.75°W. The ridge crest appears in light green, and the Lamont seamounts appear in red. The white box (vide Figure 1a) separates a model interior domain from a sponge region where outgoing baroclinic waves are absorbed. Current meter moorings (white triangles) pertinent to this analysis were located on the West and East Flanks, on the ridge at North and Central Axis locations and just off the ridge crest to the west at W1. Important topographic passages are marked P1 and P4. The tracer SF_6 was released above the ridge at location CA.

near the site of tracer release using an inverse calculation. Our model is the first 3-D numerical description of an abyssal SF_6 tracer experiment, the first of flow and transport at a spreading center ridge that extends well beyond a ridge-crest axial valley, and the first to examine motion in a bathymetric setting at ~1 km resolution where a ridge and a seamount chain are both crucial to determining regional patterns of circulation and transport.

2. Model Specification

2.1. Model Domain and Bathymetry

[9] The model domain, a nearly square region ~200 km on a side, contains the northern half of the 9–10°N EPR segment, the Lamont seamount chain, and the western end of the Clipperton Fracture Zone (Figure 1). The ridge is a consequence of tectonic plate separation at a crustal fast spreading center (10–20 cm yr^{-1}). The Lamont seamount chain consists of five named and one unnamed seamount extending 42 km to the west of the ridge. East-west oriented Clipperton and Sequeiros Fracture Zones at the northern and southern ends of the full 9–10°N segment isolate this segment from adjoining EPR ridge sections to the east. The observed dispersion pattern of SF_6 [*Jackson et al.*, 2010] (see also Figures 8 and 20) and computational resource limits together dictated the center location and size of the model domain. Not being able to include the entire ridge segment voids the model's utility for investigating topographically trapped baroclinic waves.

[10] Gridded bathymetric data were acquired from the digital archives at Lamont-Doherty Earth Observatory at 241 m horizontal grid resolution. The shallowest depth (1629 m) in the domain is located atop one of the westernmost Lamont seamounts, while the deepest point (3881 m) is in the Clipperton Fracture Zone. The depth of the ridge crest ranges from 2533 m to 2606 m within this domain. Five of the six seamounts in the chain rise above 1900 m depth, some 600 m above the shallowest ridge depth. Bathymetry over the ridge out to ±100 km at 9.6°N yields a topographic spectrum, over the length scale range 1.0 to 0.482 km, that decays with wave number k (m^{-1}) as $k^{-4.9}$. For model use, bathymetric data were regridded by averaging to a stretched computational grid having the finest zonal and meridional resolution (Δ_x = 1172 m and Δ_y = 1132 m) near the gap (P1) between the EPR and the nearest Lamont seamount. Model base depth was set to 3400 m given that 97.5% of depths in the model domain are shallower. Depths at the edges of the domain were cosine tapered over five grid cells to that base depth. Vertical grid stretching was such that the highest resolution (Δ_z = 14 m) occurred near ridge crest level.

2.2. Background Hydrography

[11] Initial and fixed boundary region stratification profiles (Figure 2) are based on CTD profiles sampled during the initial field expedition, LADDER I. Two profiles each to the east and west of the ridge by >30 km at 9.5°N were ensemble averaged and the resulting potential temperature, θ_0, and salinity, S, profiles were altered by reducing gradients near surface (z < 300 m, Figure 2), ultimately to speed computations. The model, which is focused on a description of abyssopelagic flow, does not contain the physical processes needed to sustain steep gradient hydrography in the near-surface ocean.

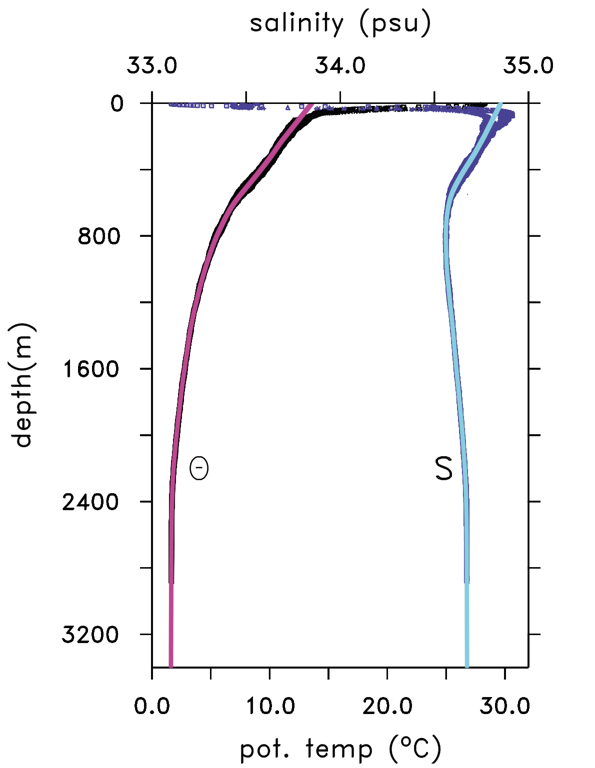

Figure 2. Potential temperature (black) and salinity (dark blue) data from four off-ridge CTD casts, with superimposed profiles (magenta and light blue) used in the model as fixed background hydrography.

2.3. Currents

[12] Currents were measured on seven moorings over the period November 2006 to November 2007 (Thurnherr et al., submitted manuscript, 2010). Meters pertinent to this study were located at Central Axis (CA), North Axis (NA), West Flank (WF), East Flank (EF), and West (W1) sites (Figure 1). Moorings NA, WF, and EF were 38 km north, 33 km west, and 39 km east of mooring CA, respectively. W1, a profiling current meter, was located 9.7 km west of the ridge crest. Time and site information for the current meters relevant to this study are given in Table 1. Current meters at all but W1 were Aanderaa RCM-11s. The meter at W1 was a Falmouth Scientific acoustic current meter mounted on a McLane Moored Profiler [*Doherty et al.*, 1999] which repeatedly sampled depths between 2300 and 2775 m as the instrument package traversed up and down the mooring line. Because CA was the site of SF_6 injection, currents observed at CA were used to construct a model forcing time series in a manner to be described later.

[13] Currents on the CA mooring at 128 m above bottom (hereafter CA-2440 m or just CA) show a strong tidal signal (Figure 3). Spectral analysis shows (Figure 4) that semi-diurnal tidal frequencies account for 35% of the kinetic energy in this record, while oscillations at periods of >200 h account for another 35%. The inertial band (50 h < T < 90 h, T_f = 71.9 h at latitude 9.8°N) and the diurnal bands account for 14% and 4% of the energy, respectively. Component analysis also shows that meridional flow on the ridge axis contains much more low-frequency energy than does the zonal component there. Off axis sites show substantially less total kinetic energy (~40%) compared to kinetic energy at site CA. Fractions of total energy for currents measured at the uppermost meter (Table 1) on mooring WF (hereafter just WF) are, for the same frequency bands, (semidiurnal) 32%, (T > 200 h) 23%, (inertial) 19%, and (diurnal) 5%.

[14] Model calculations presented here are limited to the initial 2+ month period of current meter deployments, from 3 November 2006 to 6 January 2007, a period during which the SF_6 tracer experiment was conducted. Over those 64 days, mean currents in zonal (x, u) and meridional (y, v) directions at CA were (−0.45, −0.24) cm s^{-1}. Because CA did not begin recording until 9 November 2006, currents measured at 54 m above bottom (mab) by a bottom-mounted ADCP that had been deployed earlier near CA were prefixed to the CA record to extend that record backward in time. The two current meter time series, over the overlapping time interval of 36 days, had u and v component correlation coefficients of 0.78 and 0.77, respectively, suggesting this was a reasonable extrapolation approach. Backward time extension of the CM data allowed more time for dynamical fields in the model to approach measured fields before the model tracer was injected into the system.

2.4. Model Physics and Numerical Implementation

[15] The model is a three-dimensional, time-dependent, baroclinic, hydrostatic, free-surface, f plane, primitive equation construct on a domain with four open boundaries [*Lavelle*, 2006]. At the model's spatial resolution (submesoscale −10 km to 100 m) and for tidal periods and longer, the hydrostatic assumption is likely to be good [e.g., *Zaron and Egbert*, 2006; *Mahadevan*, 2006]. At supratidal frequencies, the assumption is less clearly valid, but these frequencies contain little of the overall energy. Model variables consist of sea surface elevation η, eastward and northward horizontal velocities u and v, upward vertical velocity w, salinity (S),

Table 1. Location and Depth of Current Meters

Meter	Water Depth (m)	Meters Above Bottom (m)	Longitude (°E)	Latitude (°N)	Start Time (UT)	Length (h)
CA-2440 m	2568	128	−104.2413	9.4967	9 Nov 2006 0700	9156
WF-2481 m	2990	509	−104.5406	9.4426	31 Oct 2006 0300	9235
NA-2430 m	2502	72	−104.2917	9.8333	4 Nov 2006 0400	9326
EF-2458 m	3038	580	−103.8883	9.5530	2 Nov 2006 0500	9424
W1[a]	2785	10–485	−104.3298	9.4969	13 Nov 2006 1200	4426

[a]Profiling current meter.

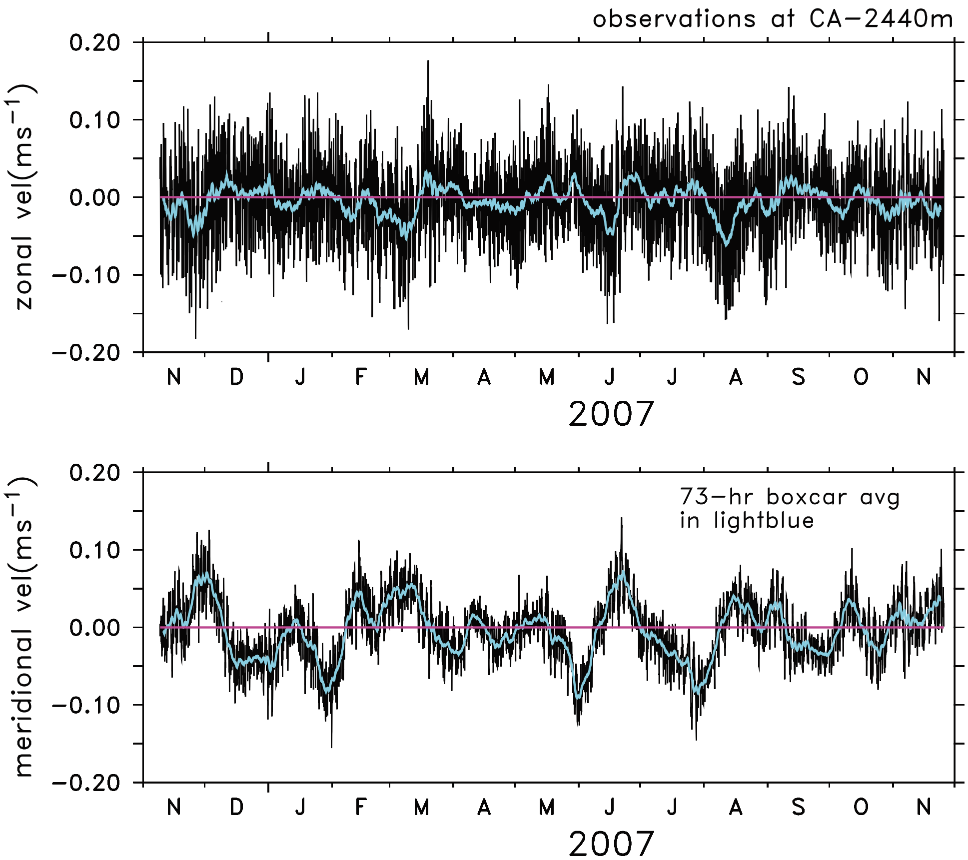

Figure 3. Zonal and meridional currents 128 m above the EPR crest at 9°30′N (Table 1, CA-2440 m) from 9 November 2006 to 25 November 2007 (Thurnherr et al., submitted manuscript, 2010). Currents boxcar averages over 73 h are shown in light blue.

potential temperature (θ_0), SF_6 tracer (C), horizontal and vertical viscosity coefficients A_h and A_Z. A_h and A_Z are linked to horizontal and vertical diffusivities K_h and K_Z through Richardson (Ri) and Prandtl (PR) numbers, the last depending on Ri [*Lavelle*, 2006]. The mixing coefficients, in horizontal and vertical directions, separately depend on fluid shear and grid size [*Smagorinsky*, 1993]. Minimum values of explicit viscosity were set to 10^{-2} m^2 s^{-1} and 10^{-5} m^2 s^{-1} in horizontal and vertical directions, respectively. The minimum vertical viscosity value of 10^{-5} m^2 s^{-1} is consistent with measurements from abyssal sites, but simulated SF_6 vertical profiles suggest that the model's implicit vertical mixing is still considerably larger. Therefore we restrict our comparisons with the tracer data to vertical integrals.

[16] The UNESCO equation of state was used for density. Outgoing internal waves generated by the model's incoming barotropic waves interacting with stratification and topography were absorbed on the periphery of the domain by the Pretty Good Sponge of *Lavelle and Thacker* [2008]. Variables u, v, η, S, and T were nudged back to either background or forcing velocities in the sponge region. Formal boundary conditions at the edges of the domain for all relevant variables were taken to be zero gradient.

[17] Equations of motion and transport were discretized over finite volumes on a z level C grid stretched in all three directions. Transport equations for T, S, and SF_6 were upstream differenced and numerical diffusion suppressed using the second-order accurate implementation of the MPDATA scheme of *Smolarkiewicz and Margolin* [1998]. The vertically averaged (i.e., barotropic, in approximation) equations for u, v, and the equation for η were solved implicitly using the pressure method, i.e., the vertically averaged u, v, and η equation set was reduced to a generalized elliptic equation for η. That equation was solved each time step by the multigrid method. Given η, u and v were subsequently determined. Time stepping was by the leapfrog method in the case of u, v, and η, and by forward time difference for S, θ_0, and C. The integration time step was 90 s. The 74 day simulation included a 10 day spin-up period, the first 2 days of which had forcing linearly ramped from rest to full value. The computational grid (x, y, z, t) consisted of 128 × 128 × 128 × 71,040 cells. Model data stored for analysis consists of arrays of the primary variables at 2 h intervals spanning a 64 day time period starting 3 November 2006.

[18] The model differs from many other regional models in that the domain is open on four sides. In addition, model forcing is determined from measured current meter data taken within the domain interior. This allows a better match of model and observations than would be possible if, for example, a basin-scale model with more limited frequency content and one not tuned to abyssal conditions were used to

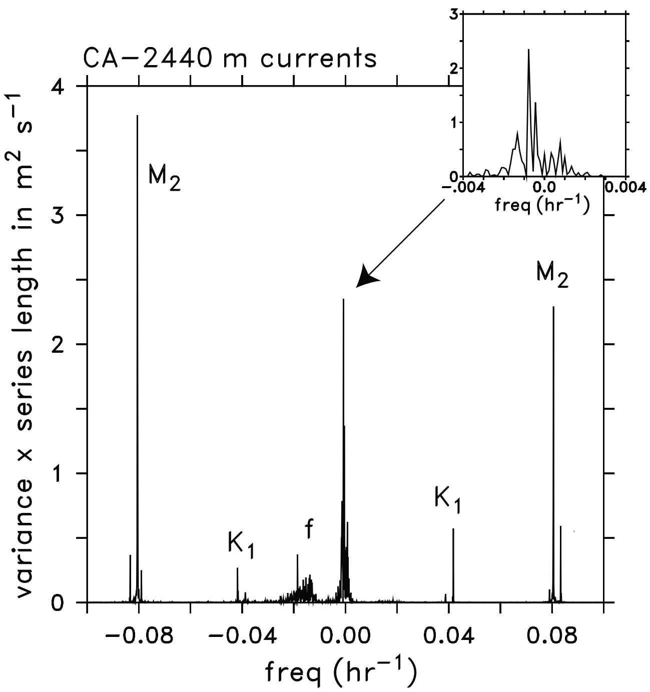

Figure 4. A periodogram, in rotary component form, of currents measured at CA-2440 m during November 2006 to November 2007. The abscissa was truncated at higher frequencies where spectral lines are insignificant at this ordinate scaling. Results are based on 9000 hourly samples. The insert shows details of the periodogram near zero frequency.

force the flow. The use of frequency components ranging from 0.5 h^{-1} to steady flow ensures that a full spectrum of motions determines model outcomes.

2.5. Model Forcing

[19] The influence of external forcing (tides, winds, etc.) on the modeled region was introduced though a body force ($\vec{F}_B$), or equivalently a spatially uniform horizontal pressure gradient (∇P_0), that caused motion throughout the domain. At large distances from ridge or other topography, a good approximation to the instantaneous horizontal momentum balance is

$$\frac{\partial \vec{v}_{\text{farfield}}}{\partial t} = -f \times \vec{v}_{\text{farfield}} + \vec{F}_B = -f \times \vec{v}_{\text{farfield}} - \nabla P_o, \quad (1)$$

where $\vec{v}_{\text{farfield}}$ is a far-field horizontal velocity, t is time, and f (2.49×10^{-5} s^{-1}) is the Coriolis parameter. Note that equation (1) lacks the quadratic bottom friction and Lagrangian interior friction terms that are present in the full model. Such terms make only a small contribution to the momentum balances in the far field above bottom, and thus it is not necessary to include them in the approximate balance used to derive the forcing.

[20] Knowledge of the v_{farfield} time series would allow an $\vec{F}_B$ (or ∇P_0) time series to be derived. If the variation of $\vec{v}_{\text{farfield}}$ were known around many points on the periphery of the model domain, then $\vec{F}_B$ could be made to vary spatially as well as temporally. The last condition cannot be met with the present (lack of) knowledge of peripheral flows, so instantaneous $\vec{F}_B$ was taken to be spatially homogeneous over the entire model region.

[21] Evaluating $\vec{F}_B$ then requires just a single peripheral velocity, but selecting a representative peripheral current velocity time series is not straightforward. Early expectations that currents recorded on moorings WF and EF, both sited well away from the ridge crest (Figure 1), would yield good forcing time series were quickly dashed. WF and EF time series, for example, were coherent at diurnal and semidiurnal tidal frequencies, but not at the longer periods important to tracer dispersal. When WF and EF time series were each used to derive model forcing, SF_6 was transported in ways and directions that made tracer results substantially unlike the observed SF_6 distribution. Because currents at the ridge crest and particularly those near the SF_6 release site would be important to SF_6 transport, particularly in its early stages, we focused on using currents measured at CA to estimate a $\vec{v}_{\text{farfield}}$ (and thus a $\vec{F}_B$) time series. The inference of $\vec{v}_{\text{farfield}}$ from currents at CA constitutes an inverse calculation, details of which are described in Appendix A.

[22] The same inverse procedure has been used in a 2-D model EPR simulation [*McGillicuddy et al.*, 2010]. In the present 3-D case, the correspondence between model and measured CA time series derived by the inverse procedure was improved by adding small constant velocity offsets, in piecewise fashion, to the inverse-derived far-field time series. The additional step primarily alters the low-frequency content of the inferred time series. We speculate that this was not necessary in the 2-D case because there the longer simulation length (~7 months) offered a larger number of low-frequency spectral lines to the inverse procedure for adjustment. In the 3-D case, the far-field ($\vec{v}_{\text{farfield}}$) time mean velocity was also adjusted to be (u_{mean}, v_{mean}) = (−3.5 mm s^{-1}, −7.0 mm s^{-1}) so that the model SF_6 was displaced far enough westward that it would more closely resemble the observed SF_6 distribution.

[23] Although the synthetic forcing time series generated by the inverse method is by no means perfect, it provides a means for matching the simulation to observations. The quality test on any model is how well its results compare with data, and the utility test of any model is whether it then provides a broader (but not necessarily complete) understanding of those measurements. The model presented herein is not the final answer on circulation and transport at this segment of the EPR, but even with the simple spatially uniform barotropic forcing used, the model provides a good deal of insight to the spatial and temporal variability of motion and transport in the region.

2.6. Model Tracer Experiment

[24] Mimicking the SF_6 field experiment [*Jackson et al.*, 2010], 3 kg of a passive tracer were introduced into the model domain over a 2.38 h period beginning on 12 November 2006 1707 UT. Tracer was released in computational cells adjacent to the seafloor over a ridge-crest track line of 1 km length, beginning and ending at (9.4928°N, 104.2447°W) and (9.5034°N, 104.2430°W) respectively. Model tracer was subsequently sampled at times and sites identical to those of field samples. Concentrations are reported in kg m^{-3} and, when vertically integrated, also as nmol m^{-2}. SF_6 has a molar

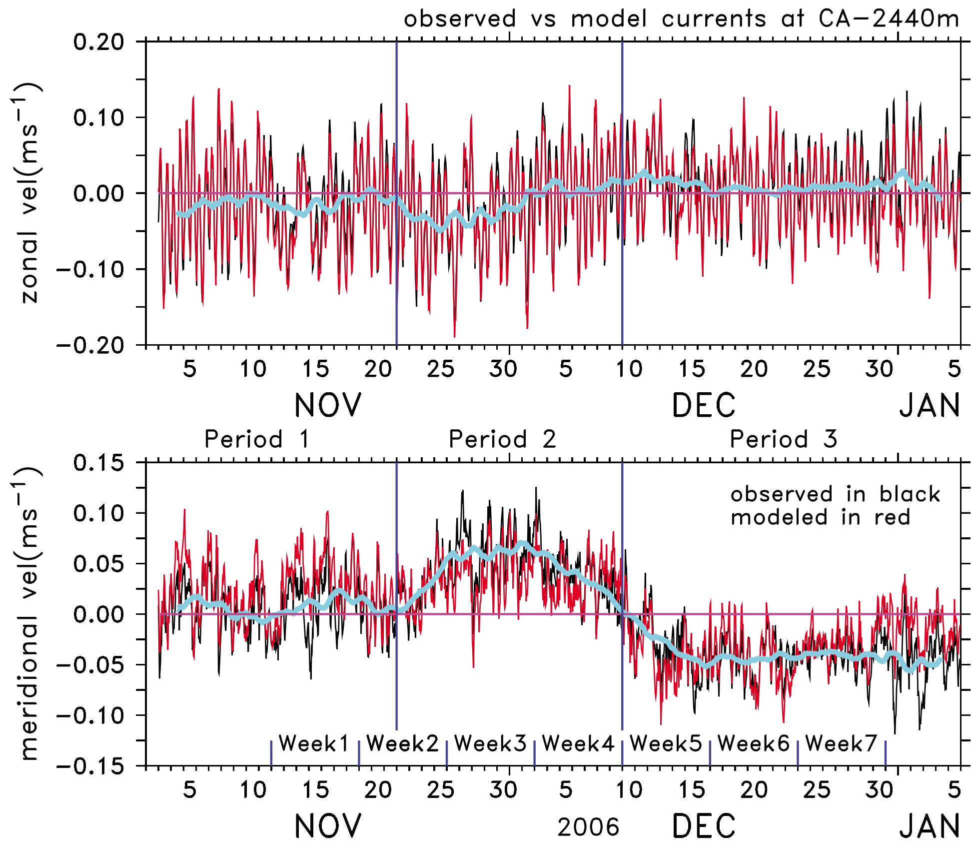

Figure 5. Observations (black) and model currents (red) at station CA-2440 m. The blue curve is a 73 h boxcar average of the underlying field data. Periods 1–3 are delineated with dark blue lines. Period 1 and period 3 roughly correspond to the LADDER I and LADDER II field periods. Shorter time periods week 1 to week 7, indicated in Figure 5 (bottom), are also referenced in the text.

mass of 146.06 g mol^{-1}. The detection limit for SF_6 in the field is approximately 4×10^{-15} kg m^{-3}.

3. Comparisons of Model Results With Observations: Examining Simulation Fidelity

3.1. Currents

[25] The inverse procedure for far-field velocities led to model currents at CA that closely resemble observations (Figure 5 and Table 2). The correlation coefficients (r) between model output and observed data for zonal (u) and meridional (v) currents at CA are 0.96 and 0.87, respectively. The slightly smaller r value for meridional flow is likely rooted in the facts that v has more low-frequency energy than u (Figures 3 and 5) and that the inverse procedure has more difficulty matching observations at the low-frequency end of the spectrum.

[26] Current magnitudes, directions, and kinetic energies together suggest three flow regimes during this 2 month time interval, regimes which are separated by blue lines in Figure 5 and labeled periods 1–3. For example, in both CA and WF records the kinetic energy in the flow before 22 November 2006 was much less than it is generally afterward. Notable in these current data is the reversal of longer-period flow from NNW (periods 1 and 2) to SSE (period 3) occurring near 10 December 2006. A similar partitioning of the inferred far-field time series shows WSW mean flow during period 1, west mean flow during period 2, and SSE mean flow during period 3. On axis at CA, zonal flow over most of the first two periods was weakly westward but changed to become weakly eastward flow after ~8 December. At CA, subtidal meridional flow was relatively weak until about 22 November 2006, it was very strong northward O(6 cm s^{-1}) over the following 15–18 days, and then it shifted to being reasonably strong southward O(−4 cm s^{-1}) for the remainder of the 2 month period. Sustained directional reversals of meridional flow occur at times scales of several weeks (Figure 3). SF_6 was released during period 1 and sampled during period 3.

[27] The correspondence between measured and modeled currents at sites WF and NA is not quite as good (Figures 6a and 6b) as that found at CA. Correlation coefficients between

Table 2. Statistics of Observed and Modeled Currents at CA[a]

	u Observed (m s^{-1})	u Modeled (m s^{-1})	v Observed (m s^{-1})	v Modeled (m s^{-1})
Minimum	−0.182	−0.190	−0.119	−0.110
Maximum	0.137	0.142	0.126	0.104
Mean	−0.004	−0.010	−0.002	0.003
Standard Deviation	0.055	0.057	0.044	0.040

[a]Statistics are based on 1536 hourly samples taken during the period 3 November 2006 0000 UT to 5 January 2007 2300 UT.

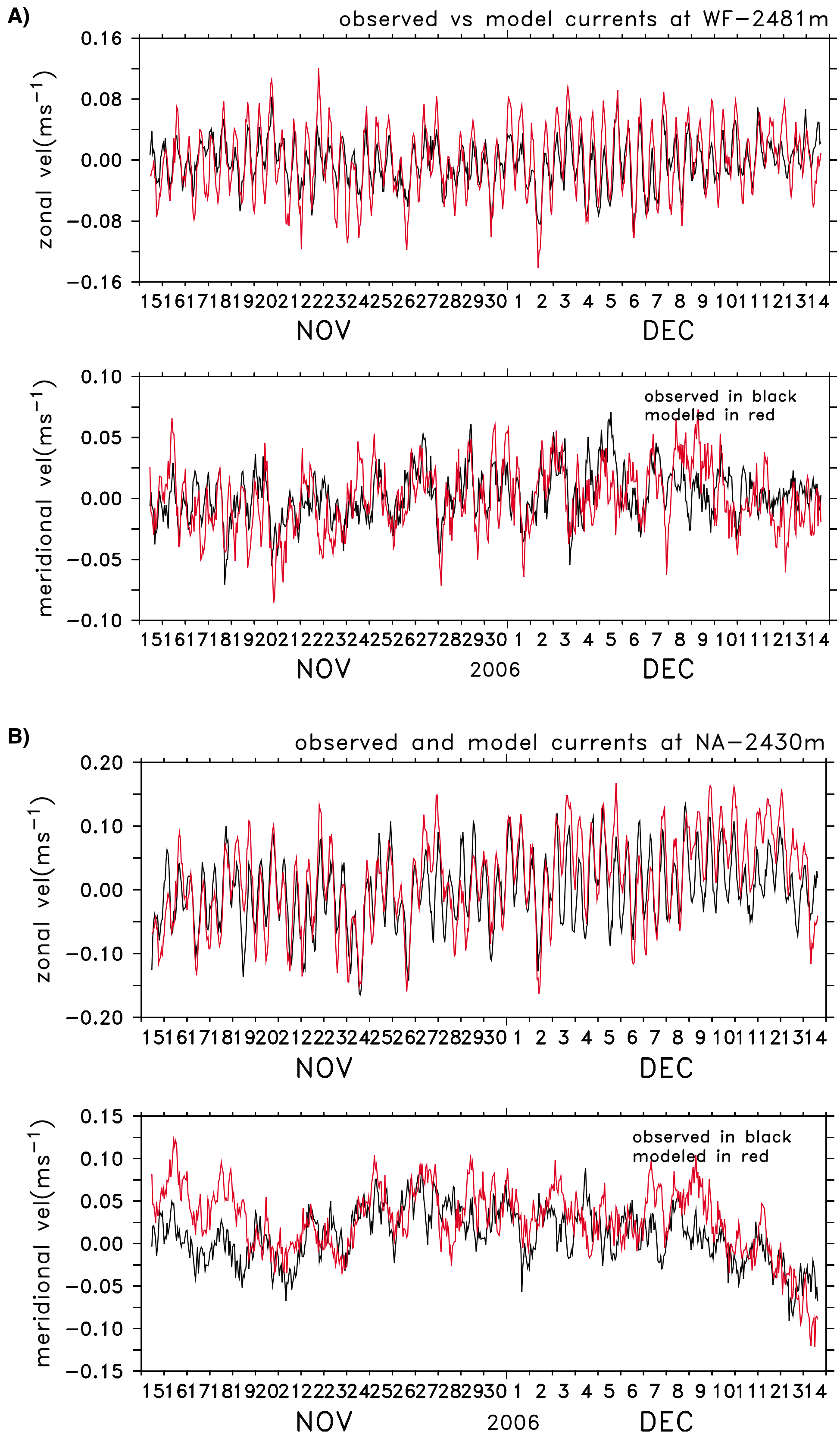

Figure 6. Comparison of measured and model time series at (a) WF-2481 m, some 40 km west of the ridge and at (b) NA-2458 m, approximately 50 km north of CA along the ridge (Table 1). Here only 29 days of the full 64 day period is plotted so that the phase matching of real and modeled time series is more clearly apparent.

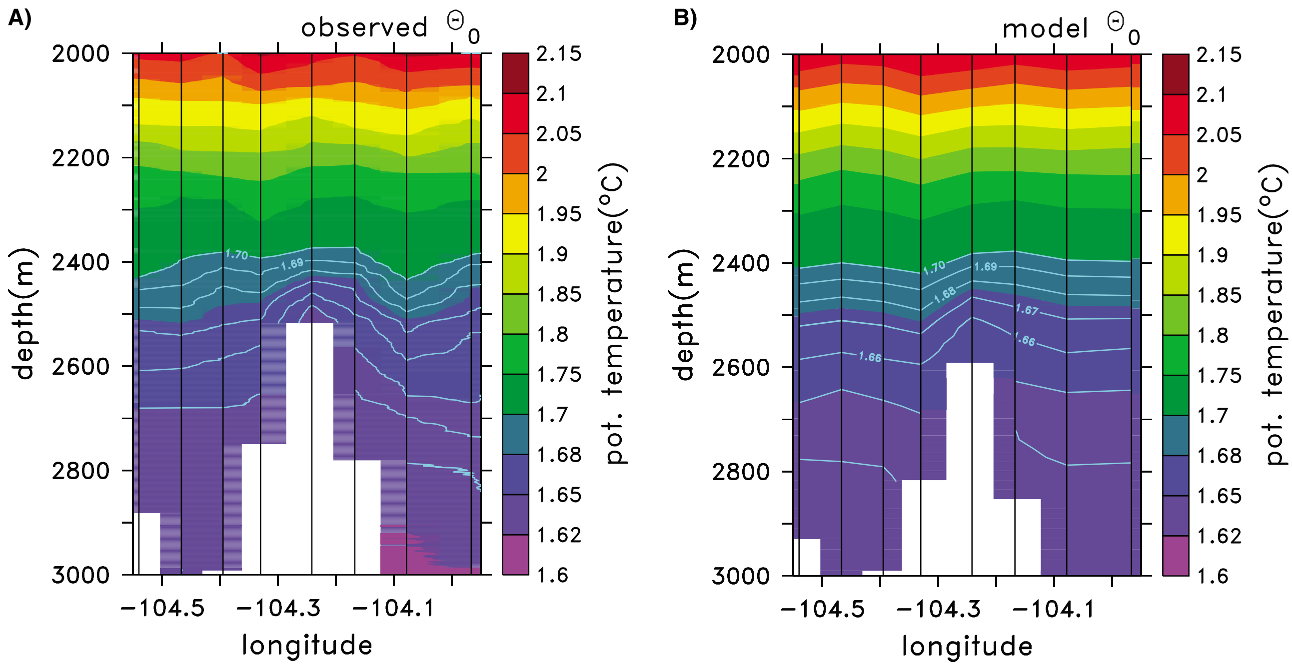

Figure 7. Transects of potential temperature across the ridge at 9°30′N. (a) Field data from a total of 20 CTD profiles that have been ensemble averaged at each of eight stations (black lines). Profiles were acquired over a 17 day period (Thurnherr et al., submitted manuscript, 2010). (b) Model data sampled at nearly the same space-time points (see text) and ensemble averaged. The difference in vertical resolution of observation and model data sets (1 m and ~15 m, respectively) leads to the apparent differences in ridge topography.

measured (u, v) and modeled (u_m, v_m) velocity components over 64 days of bihourly samples at WF are $r(u, u_m)$ = 0.74 and $r(v, v_m)$ = 0.54. At NA, the correlation values are $r(u, u_m)$ = 0.69 and $r(v, v_m)$ = 0.64. The root mean squared variance ratio for zonal flow at WF suggests model u amplitudes are too high at WF by a factor of 1.59, while at NA the same RMS ratios for both u and v are 1.33. In comparison, RMS variance ratios of model to observations at CA are 1.03 and 0.91 for u and v, respectively. Results at WF indicate that away from the ridge crest the model is overestimating current strength, primarily at tidal frequencies (Figure 6a). Too coarse resolution of the bathymetry at the crest is a possible cause, as we expect a narrower ridge would increase the baroclinic contribution to tidal currents over the ridge for the same far-field forcing (in particular, for far-field tidal currents). To match tidal current amplitudes at a narrower ridge, the model far-field tidal amplitudes would have to be reduced. Reduced far-field tidal current amplitudes would result in reduced tidal current amplitudes at WF. It was not practical to test this idea at higher resolution with the computational resources presently available to us, however.

3.2. Hydrography

[28] During the initial two weeks of LADDER I (30 October to 15 November 2006) 20 CTD profiles were collected on a transect normal to the ridge at 9.5°N (Thurnherr et al., submitted manuscript, 2010). The transect consisted of nine stations so that repeat profiles could be obtained, in some cases three times at a single station. Stations were separated by an average distance of 9.3 km, with the farthest off-axis profiles 33 km west and 41 km east of the ridge crest. The potential temperature (θ_0) data were ensemble averaged at each station and results plotted in Figure 7. Corresponding isopyncals over the entire water column are presented by Thurnherr et al. (submitted manuscript, 2010).

[29] A dominant feature in the transect is the waviness of the isotherms in the water column between 2000 m and 2300 m depth, partly indicative of the influence of internal waves, including internal tides. Two other features are notable as well: the upward bowing of isotherms over the ridge crest and the pronounced cross-ridge asymmetry of the isotherms below 2550 m. Isotherms of θ_0 rise upward above the ridge crest >100 m with respect to the depth of the same isotherm at more distant stations. Below crest depth, identical isotherms are shallower east of the ridge than to the west. During this time (period 1), regional background flow was to the WSW. Thurnherr et al. (submitted manuscript, 2010) reports related cross-ridge asymmetry in density anomalies and relates that asymmetry to the direction of zonal flow across the ridge which, during this time interval, lifts isopynals on the east flank and pushes them downward on the west flank.

[30] Model isotherms (Figure 7b) were sampled at the same locations and, when possible, time. Because the simulation begins 3 November 2006, field profiles taken before that date, six in number, were represented in the model data set by profiles taken at the time of the field sample plus 15 days. Nevertheless, the model transect shows the same main features: isotherm waviness, isotherm doming over the crest, and the east-west asymmetry of θ_0 with isotherms uplifted to the east of the ridge and set downward to the west.

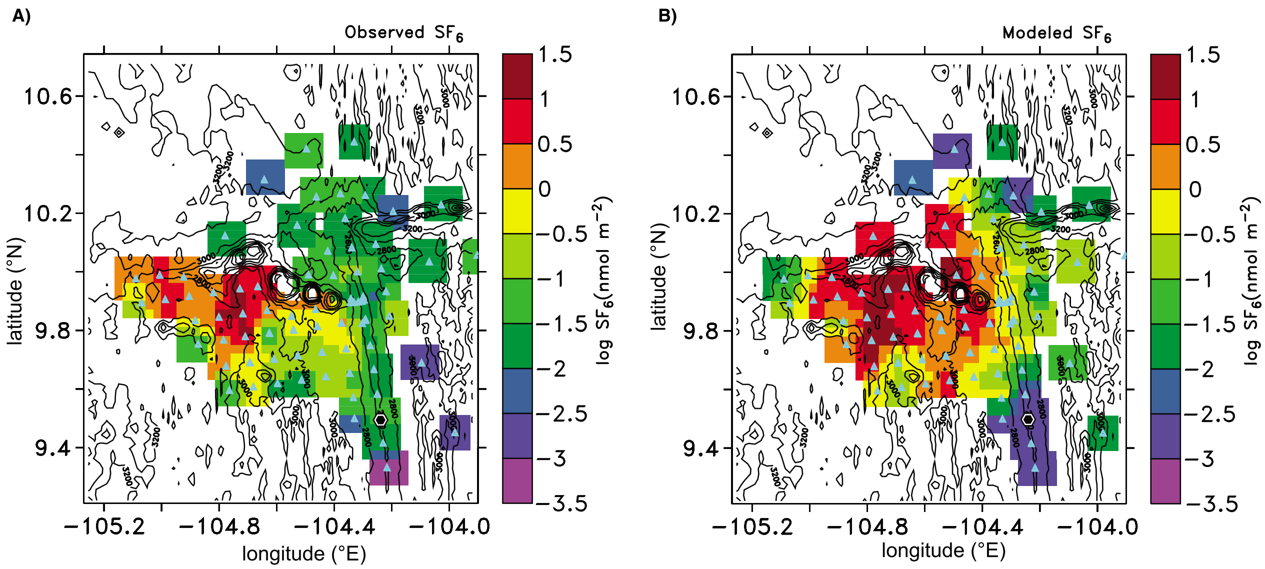

Figure 8. (a) Observed, vertically integrated SF_6 concentration data at stations (N = 90) indicated by light blue triangles. The irregularly spaced data were smoothed by objective analysis using a Gaussian weight function in two dimensions having an e-folding distance of 0.25° and a cutoff distance for the weight function of 0.25°. The mass of observed tracer has been estimated to be approximately 60% of that initially injected amount [*Jackson et al.*, 2010]. (b) Model SF_6 data sampled with an identical sequence of times and locations and then composited and smoothed in the same way as the field data. The SF_6 release site at 9°30′N is marked by a black and white hexagon.

In a setting like this one, where strong tidal and subinertial currents near steep topography occur, hydrographic fields will have substantial time variability that this time-average Figure 7 cannot represent. That temporal variability will be demonstrated in section 4.1 by Animation 2.[1]

3.3. SF_6 Tracer

[31] Between 14 December 2006 and 5 January 2007, profiles of the time-developing SF_6 plume were obtained by rosette at 100 stations [*Jackson et al.*, 2010]. To make a quantitative comparison here of observed and model SF_6 concentrations, we have condensed observed data by integrating SF_6 vertically over the water column and by compositing all vertically integrated profile results in Figure 8a without regard to their time of acquisition. The resulting plot for 90 stations within the model region show that the bulk of the SF_6 observed during the survey period was located at the western end of the Lamont seamount chain (Figure 8a). Concentrations 3 orders of magnitude less were found along the ridge at certain times, and in the region of the Clipperton Fracture Zone, but no tracer was found south of 9.5°N, and little was found east of the ridge. Since the tracer origin was at 9.5°N along the ridge, most of tracer moved north and then west or northwest after release. Figure 8a makes clear that the Lamont seamounts were an important factor in the tracer's dispersion. A much more extensive account of the observational methodology and SF_6 results are given by *Jackson et al.* [2010]. The time development of the plume will be depicted later in model-derived Animation 5.

[32] The model results (Figure 8b), sampled at identical times and locations, also show the bulk of the tracer west of the EPR and south of the seamounts, and little tracer east of the ridge or south of the injection point at 9.5°N. While the model reproduces general features of the SF_6 distributions, the model also places more of the SF_6 farther south of the seamounts than do the observations and it situates larger SF_6 concentrations just north of the seamounts as well. The comparison of Figures 8a and 8b further suggests that the western edge of the observed SF_6 plume was located farther westward and had less presence north of the seamounts than the model would have it. Also note that the model apparently underestimates the tracer concentration at the release site. The time sequence of samples shows most of those differences in concentration are for samples taken late in the field survey. The simulation suggests SF_6 returned to the ridge crest from the north after having been transported toward the Lamont seamounts (see Animation 5), so this mismatch around the source point is caused primarily by the model returning less SF_6 to the ridge than did the actual flow.

[33] The correlation of measured and modeled SF_6 vertically integrated concentrations is shown in Figure 9. The correlation coefficient r of these data is 0.57. More points lie below the perfect correlation line (in red) than lie above it, indicating that the model realization tends to overestimate the tracer mass at sample locations. A region with radius of half a degree centered at the midpoint of passage P1 (Figure 1) best exemplifies where this overestimation occurs. The correlation is better for concentrations greater than 10 nmol m^{-2}.

4. Regional Model Results with Discussion

4.1. Instantaneous Motion

[34] Flow and property fields are highly variable in space and time because of the abrupt topography of the ridge and

[1] Animations are available in the HTML.

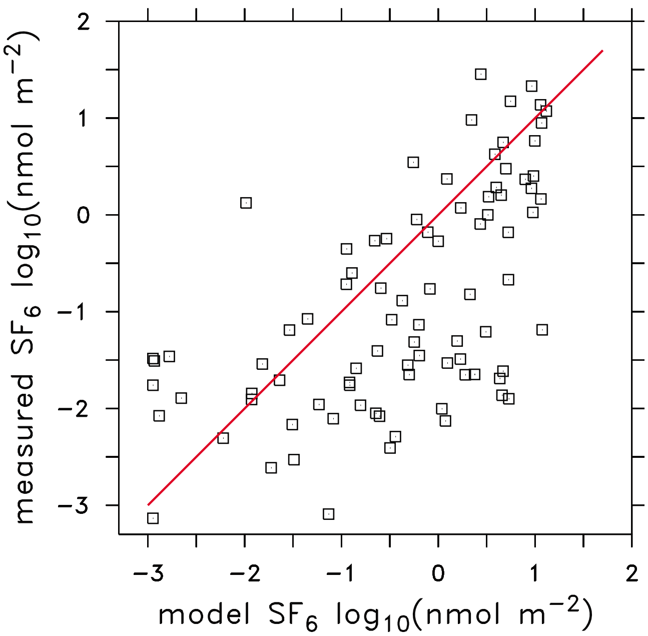

Figure 9. Model versus field measured values of vertically integrated SF_6 concentrations at 90 stations, i.e., those within the unsponged model domain. Values of log (SF_6) below −1.7 can be considered indistinguishable from SF_6 background signal. A line representing perfect correlation is shown in red.

seamounts and because impinging flows have a full spectrum of frequencies. As an example, velocity vectors at 2500 m depth during the time of SF_6 release show westward flow over the ridge rotating and intensifying as one approaches the easternmost seamounts from the south (Figure 10a). At 9°30′N currents in this snapshot (Figure 10a) have a magnitude of 11 cm s^{-1}, about 1.7 times that of the distal currents, and their direction is rotated 43° clockwise with respect to background (domain edge) current direction. At the same time and depth, larger current speeds of 19.6 and 28.0 cm s^{-1} occur in passages P1 and P4, respectively. Very little effect of the Clipperton transform fault on horizontal currents at 2500 m depth is apparent. At 2000 m depth the ridge bathymetry, muted by stratification, has little effect on currents over the ridge, as their differences with background currents in speed or direction are small (not shown). Flow intensification still occurs around the seamount at 2000 m but maximum speeds drop, for example, by ~30% through P4 as the passage widens with height above the seafloor.

[35] Potential temperatures (θ_0) at 2525 m depth (Figure 10b) show water to be colder over the ridge than anywhere else in the region at this depth. The cooler colors indicate isotherms that are uplifted over the ridge. At the other extreme, warmer colors show the consequence of vertical currents transporting heat downward from shallower depths, e.g., north of the seamounts. Uplifted isotherms over the ridge are a persistent feature while the locations of these warmer pools are time variable. Animation 1 of θ_o and currents over the time period 20 November to 20 December 2006, of which Figure 10b is one panel, shows the relatively static nature of the colder water over the ridge and, contrastingly, the relatively large oscillations of θ_0 around the seamounts and above the Clipperton Fraction Zone. Semidiurnal tidal energy is the principal factor causing the strong variability of currents and temperature in Animation 1.

[36] A zonal transect at 9.5°N at the time of SF_6 release shows flows that rise over the eastern ridge flanks and move downward on the western flanks (Figure 11a). Internal waves of the density surfaces and their associated currents are manifest. Reasonably strong westward flow occurred over the ridge crest at this time and it persisted for 36 h after the time of tracer release (Figure 11b), despite the relatively strong semidiurnal tidal currents that could have reversed the flow direction periodically over that time period. The relatively good match of model and measured horizontal currents (Figure 11b) is important to model tracer dispersion because the first few hours after release will determine which side of the ridge the tracer will initially travel. Vertical

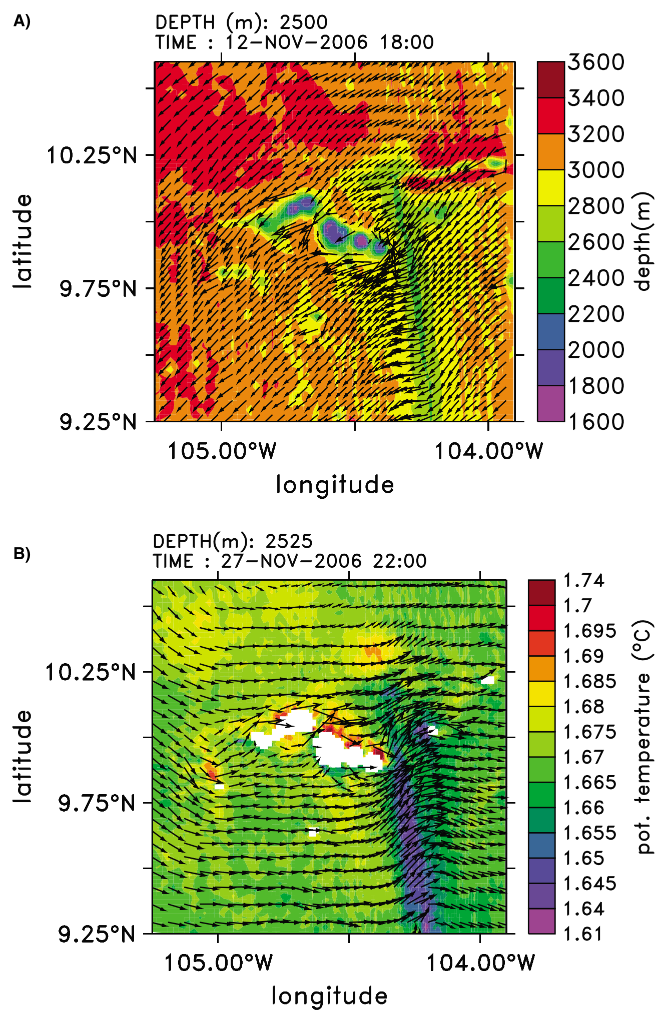

Figure 10. (a) Instantaneous current vectors at a depth of 2500 m during the time of SF_6 tracer release superimposed on bathymetry. Vector magnitudes in the lower left corner are ~6 cm s^{-1}. Vector density has been winnowed by three. (b) Current vectors at a later time at a depth of 2525 m superimposed on potential temperature. Animation 1 depicts the temporal variability of these two fields.

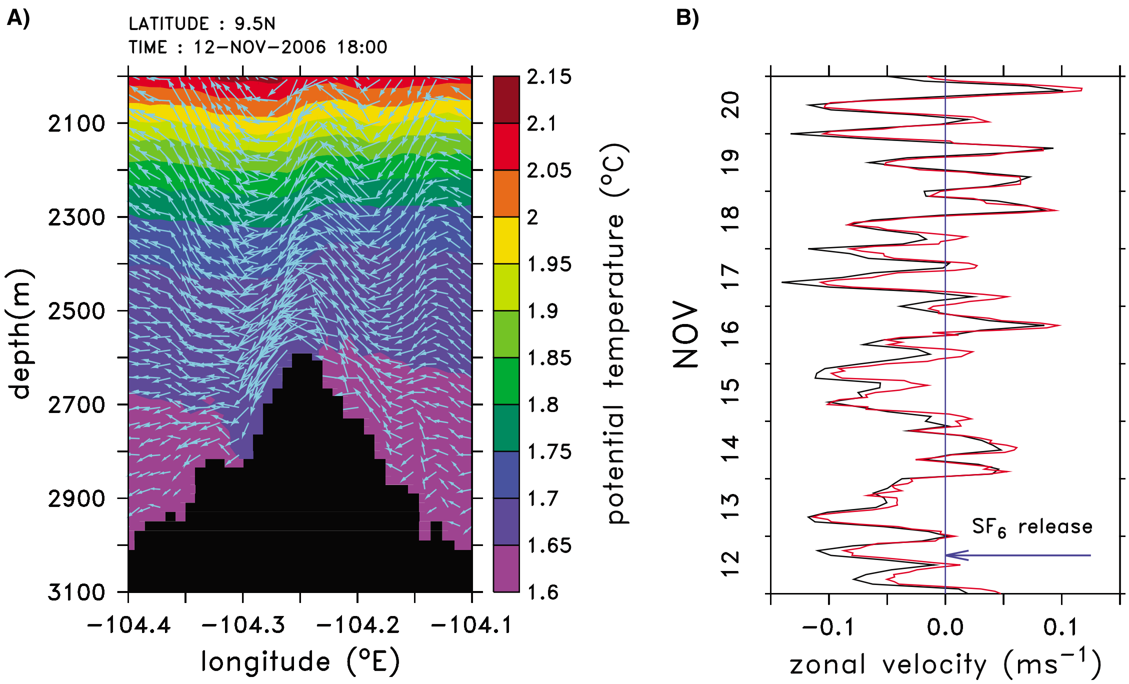

Figure 11. (a) Flow and potential temperature (in color) over the ridge at 9.5°N during the time of SF_6 release. Vectors, which have been winnowed by two in the vertical, have the same scale exaggeration as the bathymetry. (b) Measured (red) and modeled (black) zonal currents at site CA-2440 m (Table 1) at and following the time of SF_6 release (blue arrow). The current meter and SF_6 release depths differ by ~120 m.

motion is equally important because it can advect material into horizontal current jets to the side and below ridge crest depth that are important to material transport, as we will see. To give a sense of scale to w, its time series at longitude 104.275°W, latitude 9.5°N, and depth 2600 m, just west of and below the ridge crest, consisted primarily of semi-diurnal oscillations superimposed on a downward flow. The average value of w over the 36 h following the start of tracer release at that point was −0.16 cm s^{-1} with minimum and maximum w of −0.47 cm s^{-1} and +0.14 cm s^{-1}.

[37] These cross-axis/vertical flows cause, at this instant (Figure 11a), the depression of isotherms (in color) on the west ridge flank and an uplift of isotherms on the east. Isotherm asymmetry below and across the ridge as shown in Figure 11a is typical of periods 1 and 2 (Figure 5). Because Figure 11a is a snapshot, however, the vertical displacements of isotherms are exaggerated compared with a time-averaged depiction. When currents reversed to a SSE direction (period 3, Figure 5), snapshots often show isotherms that are elevated and depressed across the ridge, in the opposite sense to the ones shown in Figure 11a. Animation 2, which spans that time of flow reversal, emphasizes the tidal variations of these fields while showing longer-period flow effects.

[38] Animation 2 conveys a sense of predominately eastward propagation of internal waves. Ridge generated internal waves should propagate primarily zonally and nearly symmetrically. In this case, that near symmetry is clearly broken by internal waves generated at the seamounts. Animation 3, which depicts vertical velocity on the plane at depth 2500 m, shows internal wave motion radiating radially from the seamount region and crossing the ridge crest. It is the superposition of waves from both ridge and seamounts that determines the internal wave motion at any one point, and this superposition breaks the propagation symmetry at the ridge crest. The M_2 tidal signal is the most prominent line in the spectrum of baroclinic w, but because the model uses a broad range of forcing frequencies, internal wave ray patterns over the ridge seldom have the look of the single-frequency ideal case. A more comprehensive discussion of internal waves in this region must be left for later work.

4.2. Time-Averaged Flows Along the Ridge

[39] The high-frequency temporal variability of flow and hydrography hides important patterns that bear significantly on material (e.g., larval) transport. Transects across the ridge of time-averaged meridional flow, $\langle v \rangle$, indicate the existence of ridge-trapped jets that generally flow poleward to the west and equatorward to the east of the crest (Figure 12). Mean meridional flow is thus sheared across the ridge in an anticyclonic sense. Prior to 22 November (period 1), $\langle v \rangle$ shows a narrow northward jet with core strength >5 cm s^{-1} west of the ridge and a deeper, weaker southward jet east of the ridge (Figure 12a). Period 1 was marked by moderate WSW mean background flow (~1.2 cm s^{-1}), based on progressive vector displacement of the inferred far-field currents. After 22 November until 10 December 2006 (period 2), during which mean far-field currents were to the west at approximately the same speed, the poleward jet on the west flank (Figure 12b) intensified (mean core speed >9 cm s^{-1}). Using the $|v| = 2$ cm s^{-1} isotach to delineate an edge, the poleward jet during period 2 increased in extent to reach ~440 m above and some 20 km west of the ridge crest.

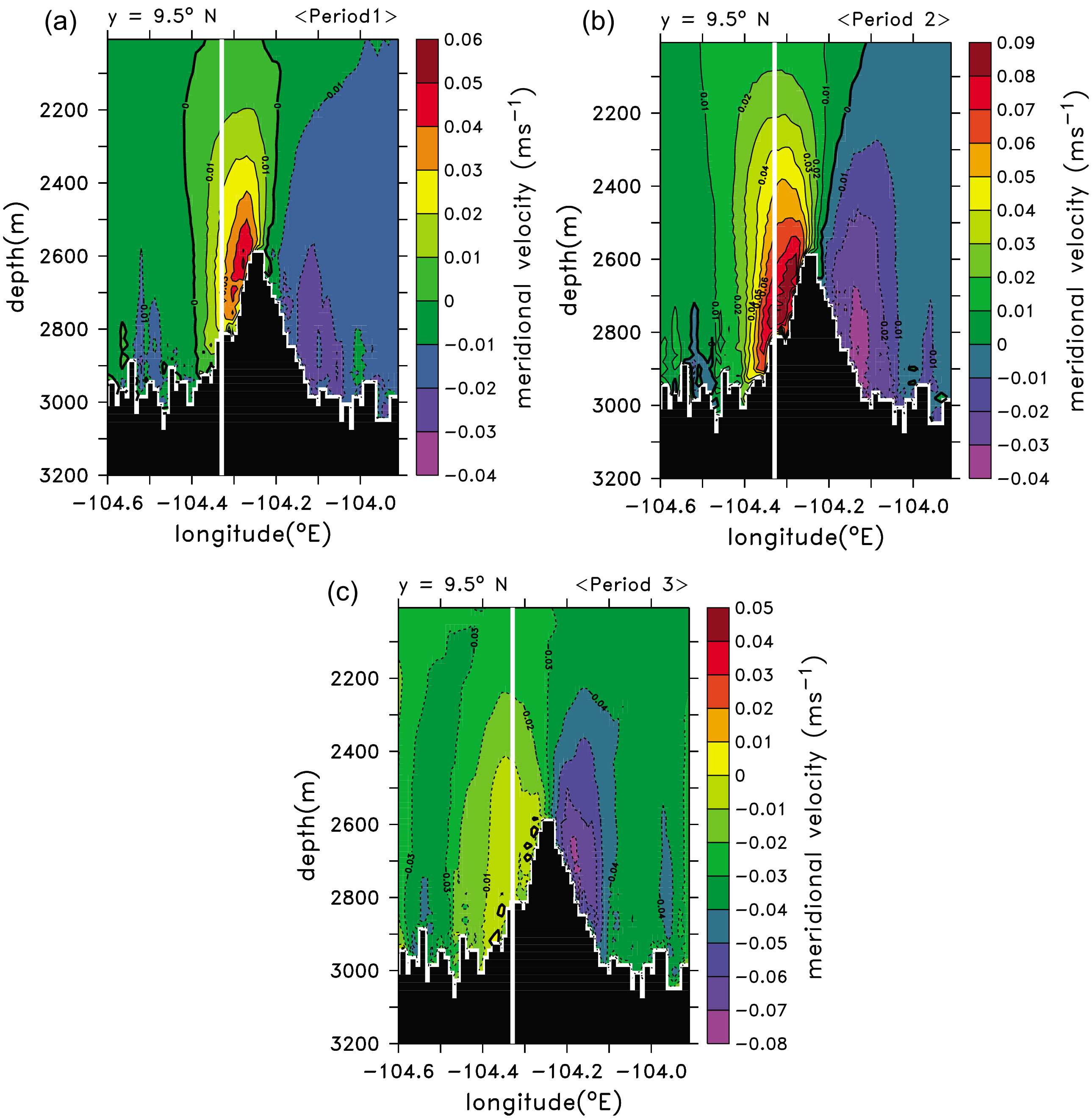

Figure 12. Meridional velocities at latitude 9.5°N time averaged over the 18–25 day time of periods 1–3 (Figure 5). Note the change in the velocity scale from period to period. The vertical white line indicates the location of profiling current meter W1.

Northward mass flux within the 2 cm s^{-1} isotach-averaged 0.61 Sv. The equatorward jet on the east flank strengthened and its core moved upward and closer to the ridge crest as well. After 10 December 2006 (period 3), when regional flow had made a large directional change to the SSE and average speed based on progressive vector displacement increased to 2.6 cm s^{-1}, consequences for the jet pattern were striking (Figure 12c). Average flow was equatorward on both sides of the ridge, though cross-ridge shear was still anticyclonic. The jet on the east flank was now as intense (>9 cm s^{-1} core strength) as the poleward jet had been during period 2, but oppositely directed, and its core was closer to the ridge crest. The size and intensity of the jets are thus related to the long-period background flow conditions, with maximum intensity for the jet pair alternating back and forth across the ridge.

[40] The 7 day averaged model profiles (Figure 13) at location W1 show some of the temporal variability of the jets that Figure 12 cannot show. Numbers in the diagram indicate the week (Figure 5) over which averages were taken, starting with profile 1 (12–19 November 2006) and ending with profile 7 (24–31 December 2006). Maximum meridional

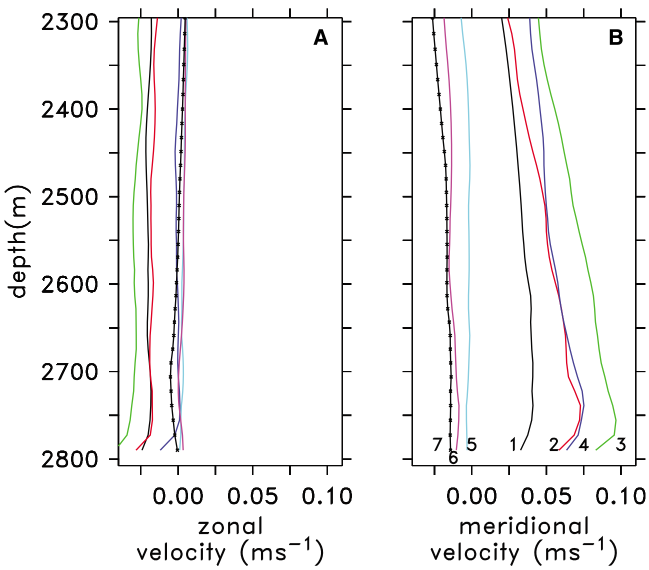

Figure 13. The 7 day averaged (a) zonal (positive eastward) and (b) meridional (positive northward) model velocity profiles at W1 (Figure 1). Averaging weeks (Figure 5) start with profile 1 (12–19 November 2006) and end with profile 7 (24–31 December 2006). Field measured profiles at W1, averaged over the same time periods, are given by Thurnherr et al. (submitted manuscript, 2010).

speed is largest in week 3 with a magnitude of ~10 cm s^{-1}. Second largest ⟨v⟩ was ~7.5 cm s^{-1} in week 4, ending 10 December 2006. Those two profiles span most of the 18 days of period 2 when meridional flow at CA was strongest to the north and when the jet reached a greater distance off ridge than in period 1 (Figure 12). Profile 2 (19–26 November 2006, week 2) includes 4 days when zonal flows at the ridge crest were strong and westerly, as they were during week 4, which may explain the comparability of profiles 2 and 4 (Figure 13). Profiles 5–7 all occur within period 3 when background currents were strongly to the SSE, the meridional flow across the entire region was equatorward, and zonal flows across the ridge were weak. Profiles 5–7 all have small zonal and meridional flow, not because meridional flows were small everywhere, but because W1 was close to the west of the ridge when mean meridional flows were at minimum and equatorward (Figure 12c).

[41] Evidence that ridge-trapped jets do occur at the EPR and have magnitudes like these comes from LADDER observations (Thurnherr et al., submitted manuscript, 2010). The profiling current meter W1, located just 9.7 km west of the ridge crest, was strategically situated to sample the poleward jet (Figure 12, white line). Thurnherr et al. (submitted manuscript, 2010) provide seven weekly averaged profiles analogous to those in Figure 13, though in their case, along- and cross-flank directions are defined with respect to local bathymetric gradients at the mooring site (320 degrees with respect to north) rather than with respect to along-ridge or meridional directions. Their profiles nonetheless show maximum along-flank speeds at W1 during weeks 3 and 4 of 10 and 7 cm s^{-1}, and across-flank flow speeds of <1.5 cm s^{-1}. Observed meridional flow grew more negative over profiles 5–7, reaching profile 6–7 extremae of ~−2 cm s^{-1}. Their profiles confirm the model prediction that flows at W1 were smaller during period 1 than during period 2 and both northward and that they were small and equatorward during period 3. A notable difference in observed and model meridional profiles is profile shape, with observed profiles showing a broader distribution of high speeds located a greater distance from the seafloor.

[42] While the W1 field observations confirm a poleward jet to the west of the ridge, the LADDER moorings cannot confirm a jet to the east because the EF mooring was too far west of the ridge. ADCP cast data, however, do provide that confirmation. Averaging cast profiles taken at different phases of the M_2 tide, Thurnherr et al. (submitted manuscript, 2010) show ensemble mean velocities during the LADDER I (approximately period 1) time period that are intensified on both sides of the ridge, poleward at a station near W1 and equatorward at a mirror image location (E1 in their notation) on the other side of the ridge crest. The equatorward flow during LADDER I was more broadly distributed zonally than the poleward flow on the westward of the ridge, as the model also shows (Figure 12a). Maximum measured core current speeds in those jets were 2–6 cm s^{-1} on the west and >6 cm s^{-1} on the east flanks, values roughly similar to those in period 1 (Figure 12a) at the cast locations.

[43] The EPR is the second ridge known to support anticyclonically sheared, ridge-trapped jets. Earlier, using current data from the Juan de Fuca Ridge (JdFR) in the northeastern Pacific at 45°N, but only at a single depth (ridge crest), *Cannon and Pashinski* [1997] had shown 3 month mean flows antisymmetrically distributed across the ridge crest with maximum speeds of 3 cm s^{-1} at distances of 10 km. *Helfrich et al.* [1998] then examined the vertical distribution of JdFR jets using additional CM data at 45°N, though only above ridge crest depth. They reported anticyclonically sheared mean flows above the ridge crest to a height of several hundred meters. Both studies built on an initial suggestion of directionally sheared mean flow across the ridge [*Cannon et al.*, 1991]. *Joyce et al.* [1998] attributed the sheared flow observed across the JdFR to a line source of buoyancy, but our model creates anticyclonically sheared jets without hydrothermal heat being present.

[44] LADDER results extend the view of ridge-trapped jets by showing that they have their largest speeds below ridge crest depth, have time-varying height and lateral extent, and have speed maxima that need not be equal or antisymmetrically located across the ridge. *McGillicuddy et al.* [2010] suggested that the interface between these oppositely directed jets sweeps back and forth across the ridge crest and infer that this is the primary reason that meridional currents measured at the ridge crest have more subinertial energy than do zonal currents, as Figure 3 shows. Maximum speeds in the EPR jets are >3 times those reported at the JdFR, but whether that is a fundamental difference, or the consequence of measuring below crest depth, and/or using shorter averaging periods in the case of the EPR, is still not known.

[45] The existence of topographically trapped jets at ridges cannot be considered surprising. Anticyclonic mean flows trapped to seamount summits in the form of toroidal circulations are well known [*Brink*, 1995]. As *Holloway and*

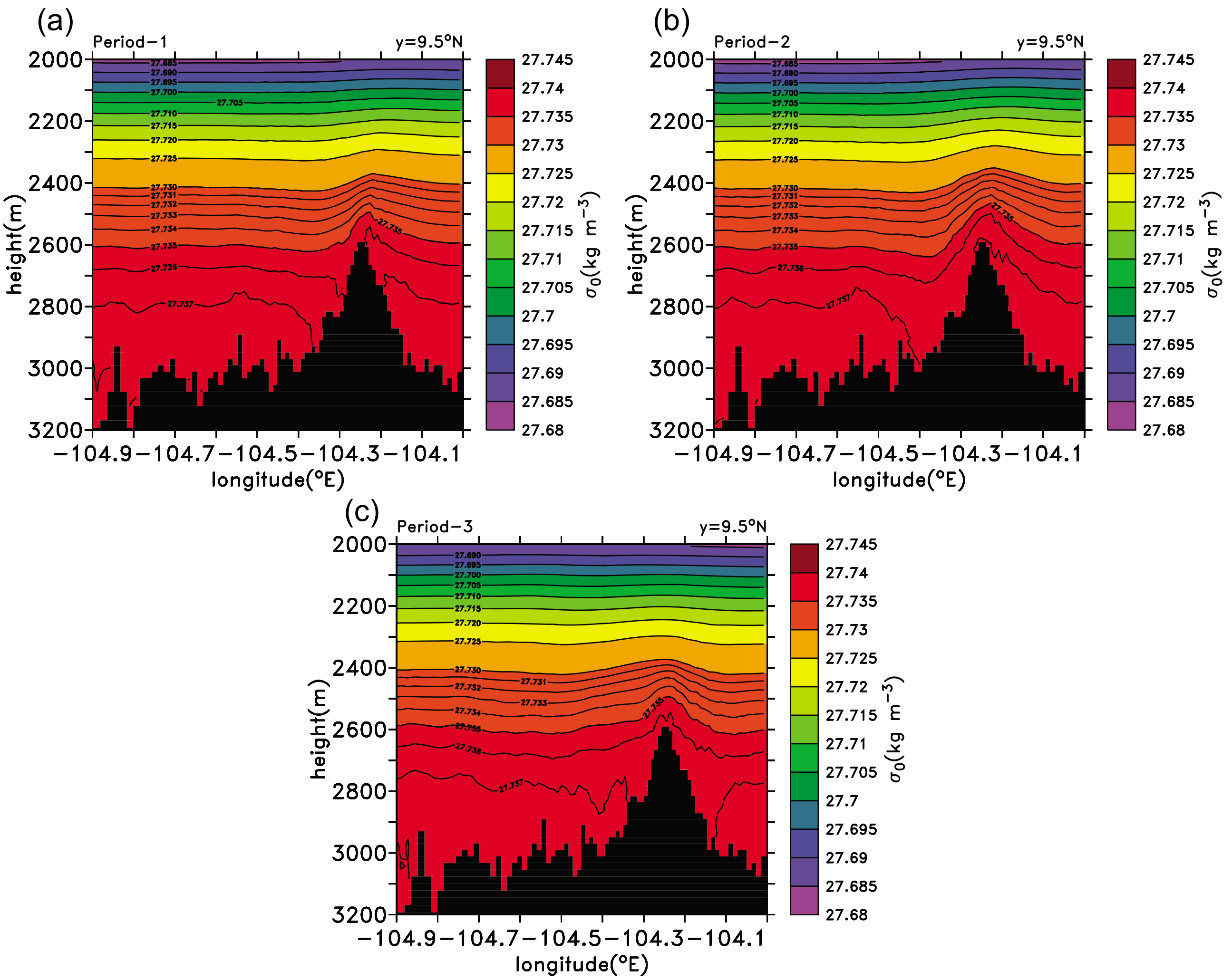

Figure 14. The 18–25 day averages of the density anomaly (σ_0) on a transect at 9.5°N for periods 1–3. The σ_0 anomalies greater than 27.73 are line contoured at 0.001 intervals.

Merrifield [1999] point out, one might think of ridges as the end point of a progression of morphologies from near-circular seamounts, to ellipsoidal seamounts, to short ridge segments, to long ridges. Anticyclonic mean flows around a seamount morph into anticyclonically sheared mean along-ridge flows in this progression.

4.3. Time-Averaged Hydrography Over the Ridge

[46] Time-averaged (2+ weeks) model potential density anomalies at 9.5°N show the accumulated effects of time-varying flow over the ridge (Figure 14). Figure 7b, in contrast, represents the average of model potential temperature data sampled 2 or 3 times at each of 8 hydrocast stations, mimicking the field sampling sequence so that model and field results could be compared. Over all three periods shown in Figures 14a–14c, each of which correspond to periods of different background flows (Figure 5), isopycnals dome upward above the ridge, elevating some isopycnals with respect to their background levels by as much as ~150 m. Doming is more subtle at shallower depths up to 2200 m. During period 1 with background flow to the WSW, isopycnals are uplifted on the east and set down on the west (Figure 14a). The same is true during period 2 when the background flow was directed to the west. During period 3, background flows were to the SSE and the result of weaker zonal mean flow over the ridge to the east is that isopycnals are more, but not entirely, symmetric over the ridge. Doming of isopycnals over some seamounts has long been recognized [e.g., *Roden*, 1987]. Doming over seamounts has been associated with a vertical circulation cell that counter intuitively brings water downward over the center of the seamount [e.g., *Brink*, 1995].

[47] Thurnherr et al. (submitted manuscript, 2010) sampled the hydrography at stations separated by ~10 km over this section during LADDER I (approximately period 1) and report isopycnals that are consistent with the depiction in Figure 14a, e.g., isopycnals that rise above the ridge ~200 m compared to the same isopycnal on the nearest cast just to the west. On the next nearest station on the east, the same isopycnal was found to lie below the level it attains over the crest and above the level attained to the west. The doming signature in the Thurnherr et al. (submitted manuscript, 2010) survey occurs up to the 2200 m level. While the WOCE line at 9.5°N [*Thompson and Johnson*, 1996] also shows doming

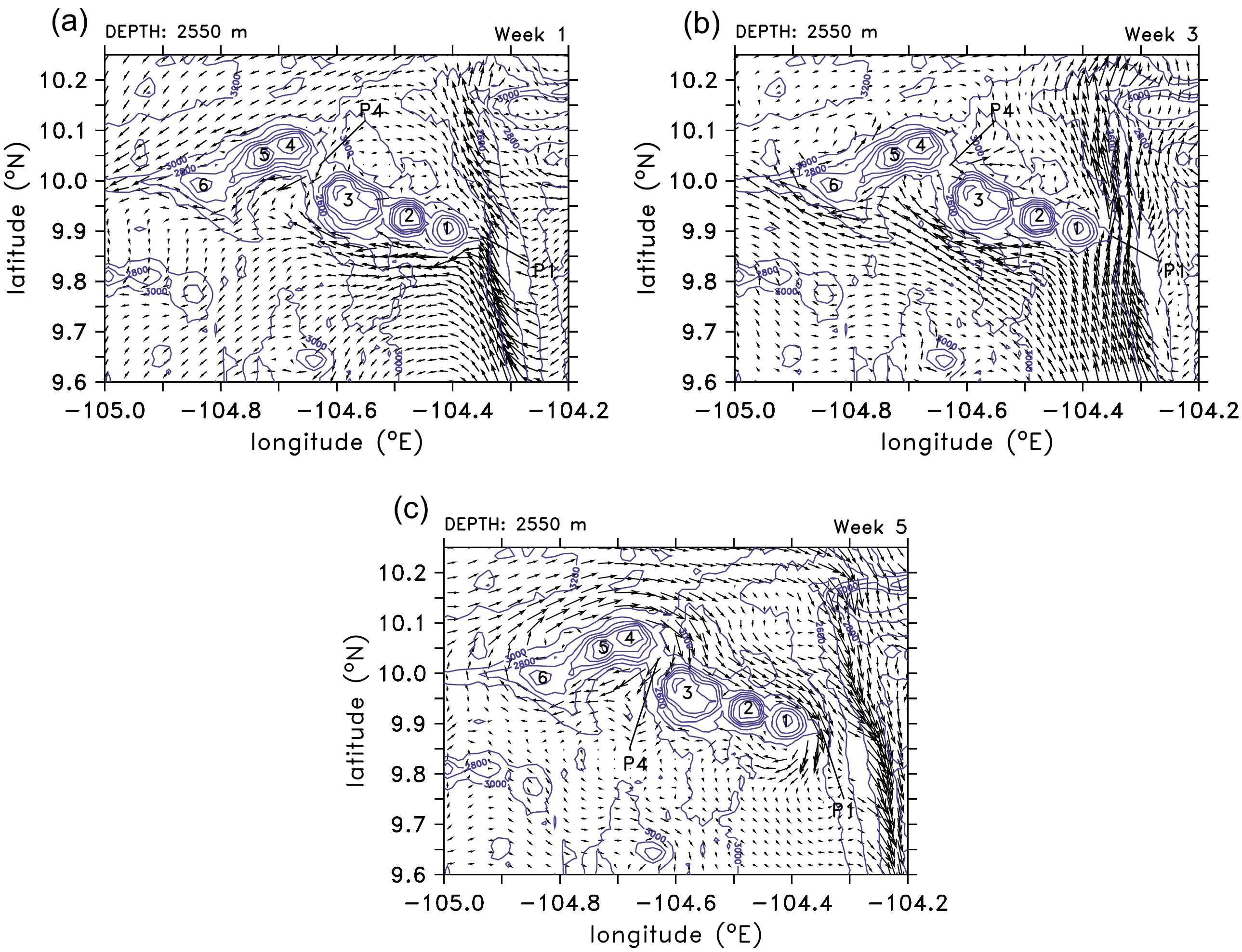

Figure 15. Vectors of 7 day mean currents during weeks 1, 3, and 5 (Figure 5), 1 week each from periods 1–3. Vector densities have been winnowed by a factor of 2 for clarity. Named Lamont seamounts are: 1, Sasha; 2, MIB; 3, MOK; 4, DTD; 5, new (all from *Fornari et al.* [1988]); 6, unnamed. The depth of the displayed currents is 2550 m. The shallowest part of the ridge has depths <2550 m and, hence, has no vectors.

above the ridge crest and plunging isopycnals on the flanks, the lateral resolution is too poor to observe the steepness of the feature present in the Thurnherr et al. (submitted manuscript, 2010) data and in model results. Hydrographic snapshots over steep topography at coarse lateral spatial resolution must thus be viewed with caution.

[48] Some of the features of the hydrography suggested by the observations and model at the EPR have analogs on the JdFR. *Cannon et al.* [1991] present transects across the South Cleft Segment on the southern end of that ridge which show doming of both potential temperature and salinity over the crest and isolines that bend downward into the flanks on both sides of the ridge. Average cast spacing was ~9 km, so the details in the hydrography were not completely resolved. A later transect over the North Cleft segment [*Cannon and Pashinski*, 1997] with average cast spacing of 4 km show isotherms higher in the water column on the east side of the ridge than on the west, some modest and broad upward bowing of isotherms at heights of 100 m or more above the ridge, and an isotherm to the east that reaches its deepest point away from and below the ridge crest. Hydrothermal heating was ascribed as the cause of the observed distribution, but in our opinion it seems more likely that it was caused by combination of heating and, as evident in Figure 14, by the flow and mixing over the ridge. The most resolved picture of hydrography over a ridge known to us comes from a tow-yow CTD section with downcasts spaced at ~1.4 km [*Cannon et al.*, 1995]. That section across the JdFR at 46.5°N shows isotherms on either side of the ridge differing in depth by as much as 80–100 m. The pattern is consistent with the measured mean cross-ridge flows of ~2 cm s^{-1}. No doming over the ridge is apparent in the *Cannon et al.* [1995] transect, which was likely affected by hydrothermal heating. *Thompson and Johnson* [1996], using a 1-D slab model configured for a slope, suggested that conductive heating and boundary layer mixing would explain isopycnals plunging downward into ridge flanks, as seen at larger scale in a WOCE hydrographic transect at 9°30′N. Our model produces plunging isopynals on the ridge flanks without employing seafloor heat sources.

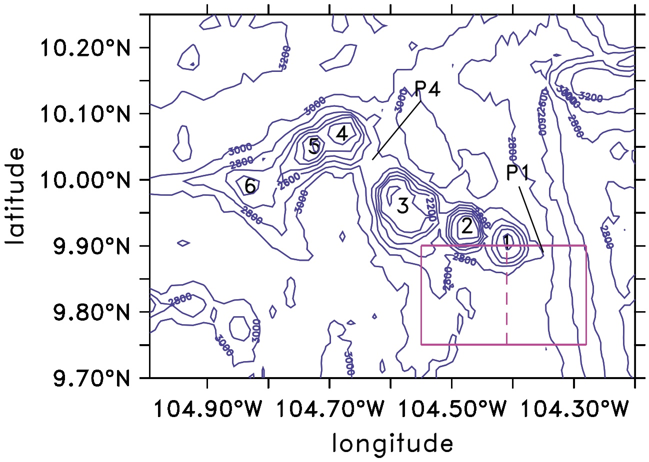

Figure 16. Location of control volumes with edges at (104.55°W, 104.41°W, 104.28°W), (9.75°N, 9.9°N), an upper surface at 2400 m depth, and lower surface at the seafloor. The large control volume is delineated by solid lines. A smaller control volume, contained within the larger one, is delineated by a dashed line on its western edge and solid lines on its other edges. Flux through lateral control volume faces are identified by compass direction and outward directed flux is positive.

4.4. Spatial Patterns of Flow Through Passage P1 and Around the Lamont Seamounts

[49] Water and particles (e.g., larvae) moving northward in the western EPR flank jet ultimately encounter passage P1 and the easternmost Lamont seamounts, raising the question as to what happens then. Circulation in the vicinity of P1 determined the trajectory of SF_6 after the tracer reached that locale, and circulation at P1 will determine the trajectory and fate of larvae in similar ways. Model results show only a fraction of poleward flow at and below ridge crest depth typically passes northward through P1, i.e., P1 is a choke point. The remaining fraction of poleward flow moves westward in a relatively narrow stream south of the seamounts, and then either around the seamounts or off into the abyss in the west. At other times (e.g., period 3), flow through P1 is entirely southward, while flow along the ridge west flank is southward as well (Figure 12c). In this section, spatial patterns in weekly averaged model data are used to examine choke point flow and flow around the Lamont seamount chain.

[50] Flow vectors at a depth level 2550 m, one weekly average from each of periods 1–3, will demonstrate some of the time and space variability of flow in this region. During week 1 (Figure 5, period 1, WSW background flow), flow was northward along the ridge south of P1, but bifurcates there (Figure 15a). The fraction of flow-passing P1 continues past the northern end of the ridge and on into abyssal depths. These vectors (Figure 15a) give no indication that flow turns southward at the northern ridge tip or that it is influenced by the Clipperton Fracture Zone.

[51] Flow directed westward at P1 on a path south of the seamounts continues westward, joining southward flow through passage P4. Flows on both north and south sides of the most western Lamont seamounts converge and continue westward into deeper water west of the chain, a second unpropitious destination for larvae. East of the EPR very little southward flow is apparent, as was observed at 9.5°N in Figure 12a.

[52] During week 3 (Figure 5, period 2, W background flow) the jet along the western ridge flank widens (Figure 12b) and the two seamounts nearest the ridge block northward passage to a seemingly larger fraction of the poleward jet (Figure 17b). Still, northward flow is strong through P1and reasonably strong westward in the region just south of the seamounts. In contrast to period 1 and 3 (as will be shown), flow is slight through passage P4 during this week. As during week 1 (Figure 15a), flow reaching the northern tip of the ridge or the western end of the seamounts continues onward into deeper water. Very little southward flow occurs at this depth level east of the ridge (as in Figure 12b).

[53] Just after background flow turns to the SSE (week 5, period 3, Figure 5) weekly mean flow vectors have a much different look (Figure 15c). Flow is strongly equatorward on the eastern side of the ridge. Moreover, flow through passage P1 is strongly southward. Circulation is anticyclonic around the entire Lamont chain and anticyclonic around the smaller edifice formed by the three most western seamounts, numbered 4, 5, and 6 (Figure 15c). This flow pattern increases the probability of fluid or particles situated north of the seamounts returning to the vicinity of the ridge. At shoaler depths, the size of these anticyclonic flow structures shrink (not shown). At 2200 m depth, flow circles the composite peak of 4 and 5 anticyclonically, but traverses the top of seamount 6. At 2000 m depth, the saddle between seamounts 4 and 5 is breached by flow, and anticyclonic circulations around each begin to appear. Anticyclonic flow circling seamounts 1, 2, and 3 might set up conditions for considerable lateral shear in the passages between them, but the model cannot presently resolve conditions in the passages between seamounts 1 and 2 or 2 and 3 with sufficient resolution to say so.

[54] Animation 4 which is of weekly average flow vectors sampled daily shows some additional transitory features. In Animation 4, flows east of 104.4°W have been color coded so that poleward flows are red and equatorward flows are blue. Animation 4 points out the large temporal variability in even weekly averaged data. Anticyclonic eddies are occasionally evident in topographic pockets, especially south of and between seamounts 1 and 2, SW of seamount 3, and NW of the saddle between seamounts 5 and 6. The second feature to note is strong equatorward flow west of the ridge crest that develops in the later part of December in response to persistent SE background flows.

4.5. Flux Through Passage P1 Versus Westward Flux South of the Seamounts

[55] The partitioning of flow into a westward branch south of the seamounts versus a northward branch through P1 is examined via a flux calculation using the two control volumes (CV) outlined in Figure 16. A large CV is bounded by the solid lines. A smaller CV occupies the eastern end of the larger CV and is bounded on the west by a dashed interior line (Figure 16) and otherwise by solid lines that contribute to the outline of the larger CV. The eastern control surface of both CVs sits on top of the ridge, the upper control face of both is located at a depth of 2400 m, 150 m above

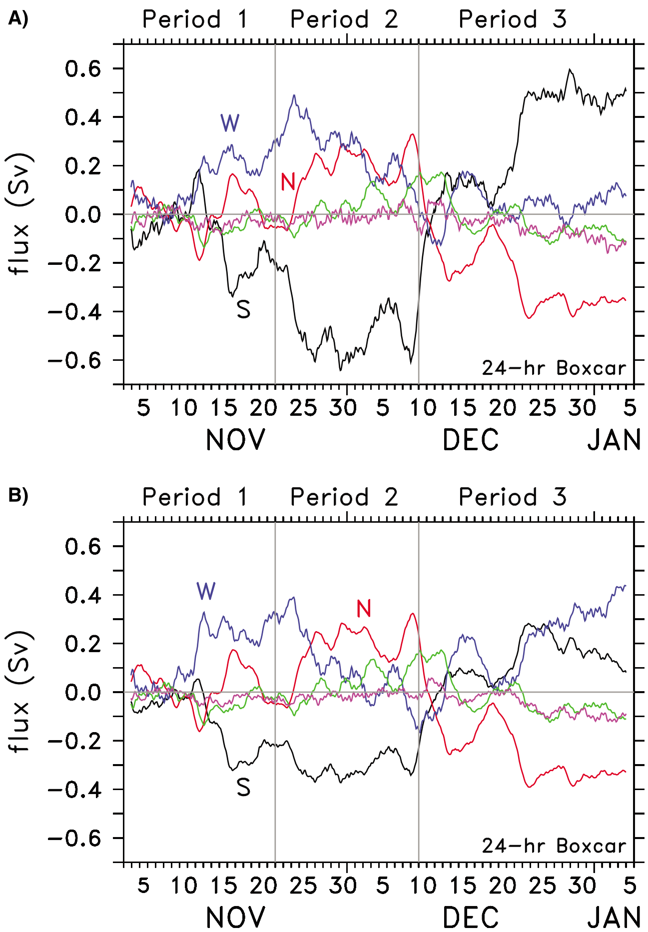

Figure 17. Time series of model fluxes (a) through the large control volume surfaces and (b) through the small control volume surfaces (Figure 16). Fluxes through the S, N, W, E, and top surfaces are colored black, red, blue, green, and magenta, respectively. The time series have been smoothed with a 24 h boxcar window. Outward directed flux is positive.

nominal ridge crest depth, and the lower face of both is the seabed.

[56] Fluxes of primary interest are those through the north, south, and west faces of these CVs. Fluxes through the top face and eastern face of the control volumes are relatively small. In addition, the flux through the north face of both boxes occurs primarily through passage P1 because northward fluxes through passages between seamounts 1 and 2 and between seamounts 2 and 3 are small in comparison. Time series of flux through the southern, northern, and western control surfaces for the larger CV (Figure 17a) and the smaller and eastern CV (Figure 17b) are color-coded solid lines in black, red, and blue, respectively.

[57] Fluxes during period 1 (background flow to WSW) in the two sets of time series are fairly similar, suggesting that most of the flux from the south entered through the south face of the smaller CV. Also, during this period the flux through the west face of the smaller CV passed onward through the west face of the larger CV without much loss between. During period 1 the time integrated north face flux was only 14% of the west face flux, however. Moreover, north face flux was negative over 45% of that time period.

[58] During period 2 (background flow to the west), flux from the south into the large CV was very much larger than in the previous period. Only about half of this flux was across the south face of the smaller CV. This result is consistent with the vector depiction in Figure 15b, showing a much wider meridional jet approaching the seamounts. The fluxes through the north faces of both control volumes were positive over nearly the entire time period. The most interesting difference between the Figures 17a and 17b during period 2 is in the fluxes through the western faces. The flux through the western face of the smaller, eastern CV drops toward small values around 27 November 2006, but flux through the western face of the large CV declines more slowly in magnitude. The loss of flux through the dashed line CV face is compensated by flux through the western half of the southern face of the large CV. After 27 November 2006 nearly all the fluid coming into the smaller CV from the south leaves that CV to the north, until the situation changes around 10 December 2006.

[59] Fluxes through the northern (red) and southern (black) faces of both control volumes are equatorward in period 3 (after 10 December 2006). The flux through the western face of the large CV is smaller than through the western face of the eastern CV during this period because of loss to the south. Large flux from the north through passage P1 continues to the south, as Figure 12c demonstrates.

[60] Based on these time series, we infer that under conditions similar to period 1, fluid coming from the south along the ridge will move primarily westward on a course south of the seamounts rather than through P1. Under conditions prevailing in period 2, northward flux through P1 is much larger. The flux times series for the smaller CV shows that that 59% of the fluid passing the southern face of the smaller CV passed northward through P1 during period 2, most of the occurring after 26 November. The small flux through the west face of the smaller CV during period 2 after that date contrasted with the relatively large west face flux through the larger CV over the same interval indicates that the broad, northward flowing ridge trapped jet (Figure 15b) was split, south of the P1 and adjoining seamounts, into a northward and a westward flux fractions. Much of the eastern part of the northward flowing jet continued through P1 while the western part of the northward flowing jet, having its northward motion blocked by the Lamont seamounts, turned west.

[61] Between 20 and 24 November (spanning the transition between periods 1 and 2) flux thorough P1 was temporarily southward. During that time period fluid in the smaller CV traversed westward. Once that fluid had passed the westward face of the smaller CV, it continued westward through the west face of the large CV. This is the sequence of events that likely affected the dispersion of SF_6, as will be discussed in section 4.6.

[62] The north face flux though P1 over the entire 64 days, without filtering, is reproduced in Figure 18 (blue). The series shows flux primarily to the north over the first 60% of this record and then flux to the south over the remaining 27 days. Overlaying the model flux time series is the meridional velocity time series measured at CA (Figure 18, black).

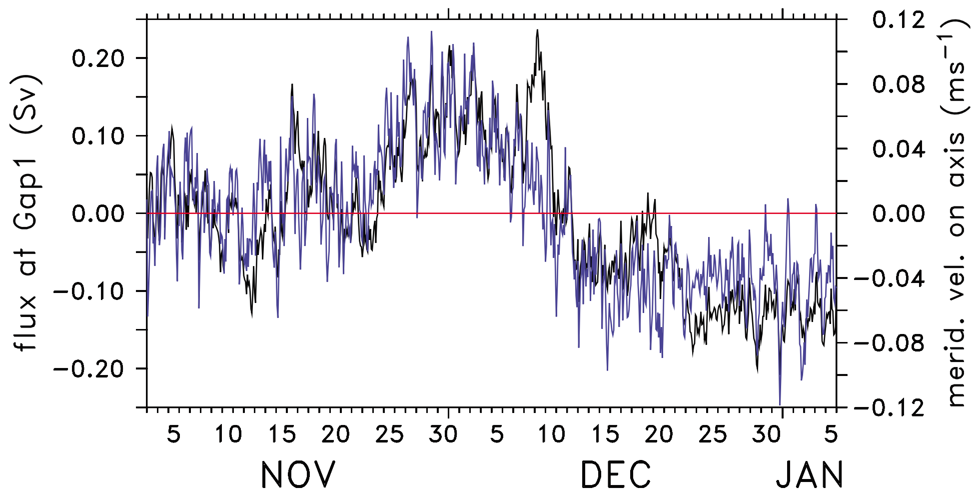

Figure 18. Flux (in blue) below nominal ridge crest depth (2550 m) through passage P1 superimposed on meridional currents measured at CA-2440 m (in black).

The two time series are clearly correlated (r = 0.84). The relationship suggests that the magnitude of northward meridional currents at CA is an indicator of the magnitude and direction of flux through P1. Measurements at CA can thus be used to gauge the flux rate and transport direction through P1. The full year time series of v at CA (Figure 3) and this correlation suggests that meridional transport at P1was equatorward >54% of the year beginning November 2006. When period 3-like conditions do not prevail, poleward flux will bifurcate south of P1, one branch to go westward and the rest northward to the ridge's northern tip and beyond. The odds of larvae that approach P1 from the south in the west flank jet passing northward through the P1 choke point are less than even.

4.6. SF_6 Dispersion During the Tracer Experiment

[63] The LADDER SF_6 field experiment [*Jackson et al.*, 2010] was simulated using a passive tracer, released at the same time and place of the actual SF_6. This model calculation was undertaken to assess the quality of model transport, to infer the SF_6 trajectory between the times of injection (12 November 2006) and initial samples (begun 14 December 2006), and to interpolate and extrapolate the SF_6 field data thereafter between scarce and scattered points. The differences in measured and model SF6 distributions (section 2.3), particularly in the fraction of tracer mass observed north of the Lamont seamounts, however, should be a reminder that the model can only coarsely identify important transport patterns and pathways but not the complete transport history of the actual tracer.

[64] Model results suggest that in the first few hours after tracer release the SF_6 moved westward and down the western ridge flank (Figure 19a). Vertical flow down the flanks proves to be important. Approximately 6 h after release 5% of the tracer was already situated below 2600 m. At 36 h and 5 days, 90% and 98% of the tracer, respectively, integrated over latitude and longitude, was located below 2600 m. Entrainment into buoyant hydrothermal plumes (not considered in this calculation) would be one mechanism for keeping some tracer (and larvae) away from the strongest of those downward vertical flows and above ridge crest depth.

[65] At 36 h, the maximum tracer concentration was located at latitude 9.54°N (Figure 19b), implying a mean poleward advection speed of ~4.8 cm s^{-1}, a value consistent with speeds in the transect during period 1 (Figure 12a). At 5 days, maximum SF_6 concentration integrated over depth and longitude was located at 9.73°N (Figure 19c). Thus, initially SF_6 moved down and along the western flank to the north. Five days after release, the locus of maximum tracer concentration had separated from the ridge and extended to the seafloor (Figure 19c). Tracer concentration at 5 days, integrated over depth and longitudes and fit with a Gaussian distribution, suggest an effective along-axis diffusion coefficient having a magnitude of 40 m^2 s^{-1}. Potential density contours in Figures 19a–19c show the consequences of westward zonal and accompanying vertical flow (Figure 11a).

[66] Vertically integrated SF_6 concentrations (kg m^{-2}) at 7.3, 32, and 45 days past tracer release (Figure 20), shows the plume's subsequent development. At 7.3 days (20 November 2006 0000 UT), the SF_6 plume core has reached the choke point P1 and the first Lamont seamount. The core of the plume at this instant is located ~11.5 km west of the ridge crest and Figure 20a shows a minor amount of the tracer traversing northward through passage P1. The mass north of seamount 1's central latitude (9.91°N) at this time is <1% of the initial mass, however. Three days later the same calculation shows a value of <0.7%. At 7.3 days, the mass of tracer west of seamount 1's central longitude (104.41°W) was 30% of the initial mass, but 3 days later the value had increased to 88%.

[67] By 25 November 2006, tracer south of the seamounts had begun to pass to the north through the three channels between seamounts 1–4. On 1 December 2006 (Figure 20b) the bulk of SF_6 is found far to the west of the ridge and south of the seamounts. By then 99.5% of the original tracer mass was west of seamount 1's central longitude, and only 0.3% was located north and east of seamount 1's center.

[68] At 32 days (14 December 2006 1200 UT) at the time of the first field sampling for SF_6, the center of mass of

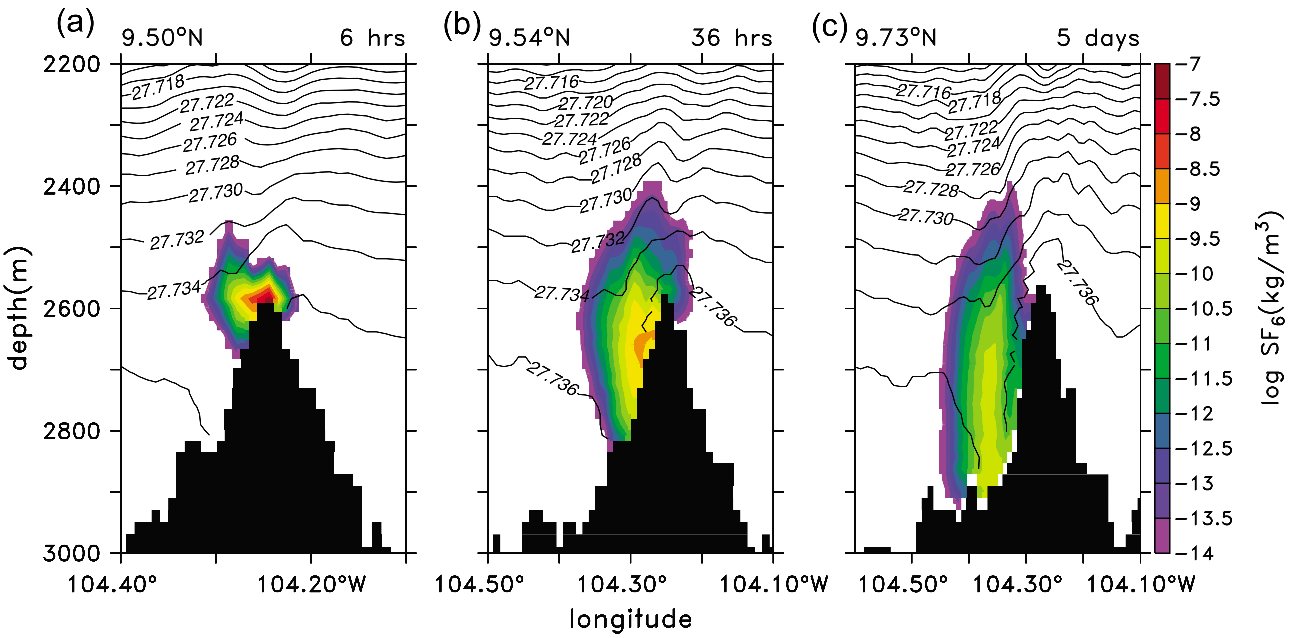

Figure 19. Cross sections of model SF_6 concentration (log scale) at latitudes of largest concentration at 6 and 36 h and 5 days after tracer release. Line contours are potential density. Abscissa scale varies.

the model SF_6 plume had moved toward the west end of the Lamont chain and approximately equal portions of the plume were found north and south of the seamounts (Figure 20c). Flow northward around the western end of the seamount chain accounted for most of the tracer mass north of the seamounts. On 14 December 2006, the circulation was already 4 days into the period 3 flow regime with background flow to the SSE. Figure 15c shows that the weekly averaged currents were then configured to advect the tracer anticyclonically around the entire seamount chain, around the edifice formed by seamounts 4–6, and likely around seamounts 1–3, though model resolution is not adequate to say that definitively.

[69] A more comprehensive picture of the vertically integrated plume evolution is found in the accompanying Animation 5, where time steps are bihourly and where field SF_6 sampling locations appear irregularly in time as light blue triangles.

[70] Animation 5 depicts several noteworthy features of transport not apparent in Figure 20. One such feature is that all the passages in the Lamont seamount chain west of seamount 1 transport tracer north to south at times and south to north at others. Even the narrowest of the passages between seamounts 1 and 2 and 2 and 3 show this exchange transport. The sequence of patterns in Figure 15 suggests little chance of northward transport through P4 but the SF_6 Animation 5 suggests otherwise. A closer look at the flow through P4 showed numerous passage-wide flow reversals during this 64 day study period as well as the suggestion of cross-channel shear in the horizontal flow. This last might be expected as the consequence of the superposition of separate anticyclonic time-averaged flows around seamount 3 and around the combined edifice of seamounts 4, 5, and 6 particularly during period 3. The background flow reversal of ~10 December caused much of the tracer to be transported northward around the western end of the seamount chain. That action, combined with the much less sizable flux of SF_6 northward through the passages between the seamounts, positioned the SF_6 to move eastward and back toward the ridge in the anticyclonic flow pattern represented in Figure 15c. Animation 5 shows that some SF_6 is reintroduced to the ridge area in this way. While Figure 15c suggests westward flow south of the seamounts during the same time period, note that this westward flow is confined to a narrow region south of the seamounts. Figure 15c suggests that transport of tracer farther south beyond that band during at least part of period 3 would have been weak and disorganized or even eastward.

[71] Mass flux of SF_6 (kg s^{-1}) through the large control volume (Figure 16) faces suggests that almost all of the SF_6 initially traveled west on a course south of the seamounts. Those time series (Figure 21) show that the only significant SF_6 fluxes in period 1 and 2 were through the south and west control volume faces. Peak flux of SF_6 crossing the south face of the large CV occurred within a week of the tracer release, and peak flux through the west face occurred about 6 days later. Time integrals of the fluxes in Figure 21 show that 97% of the initial SF_6 mass released (3 kg) passed northward though the south control face by 3 December and 95% has passed westward through the west control face by 10 December. The mass of SF_6 located within the large CV at any time (Figure 21, purple) shows a peak value on 21 November 2006 2000 UT of 2.32 g (77% of the initial mass). While SF_6 continues to flux into the CV through the south face after that time, SF_6 had begun to be transported through the west face at nearly the same time. By 30 November 2006 and continuing through 10 December 2006, the mass of SF_6 remaining in the control volume was only 0.8% of that originally injected, with most tracer located farther to the west.

[72] After 10 December 2006 (period 3), when the regional currents reversed direction, Figure 21 (red line)

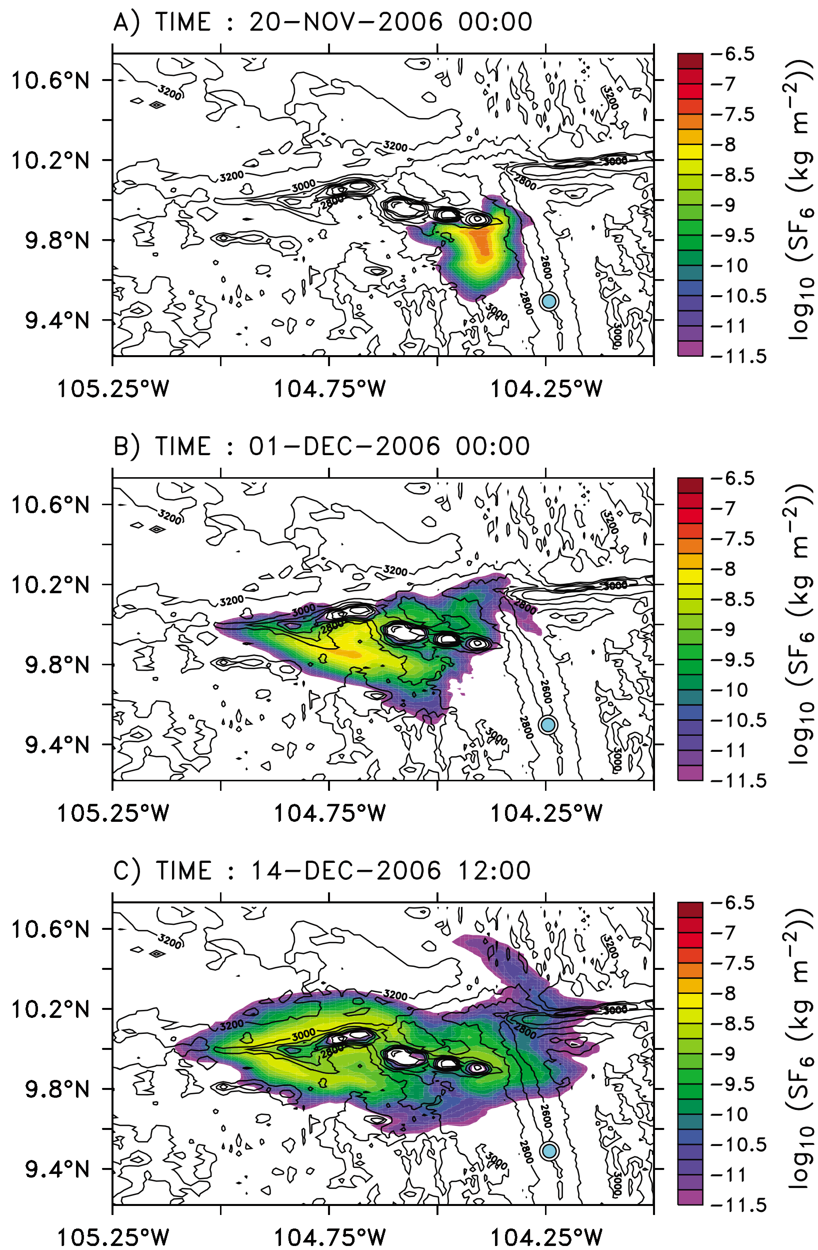

Figure 20. Vertically integrated SF_6 concentration (kg m^{-2}) on a log scale from the model at increasing times. Plume sampled at (a) 7, (b) 18, and (c) 31 days after the tracer release, the location of which is marked with a cyan circle. The first plume sample in the field was taken 14 December 2006 1200 UT corresponding to the time of Figure 20c. The smallest concentration contour represents the approximate detection limit, when vertically integrated over a 500 m depth interval.

shows SF_6 entering the control volume from the north primarily through passage P1 at a rate, when time integrated over period 3, that accounts for 20% of the SF_6 release mass. The model also suggests that 98% of the SF_6 that reached the vent field at 9°50′N on the ridge before 6 January 2007 arrived, after advection around or through the seamounts, more than 31 days after its release at 9°30′N.

[73] That SF_6 was transported so exclusively westward in the initial weeks of the experiment appears to have been more coincidental than typical. Figure 21 shows that SF_6 accumulated in the large CV up to 20 November 2006 when stored SF_6 mass reached its peak. Figures 17a and 17b show that on that very same date, fluid flux through the north face of the CVs reversed sign and fluid thorough P1 began to flow slowly southward, a circumstance that prevailed for 4 days. Time-averaged vectors show that all the poleward flow from the south along the ridge was turned westward during those 4 days. That flow then transported the SF_6 toward the western end of the CV. Figure 21 shows that the tracer began to be exported from the large CV on 23 November 2006. A day later, flow conditions had changed to be those of week 3 (Figure 15b), and while fluid flux through P1 was

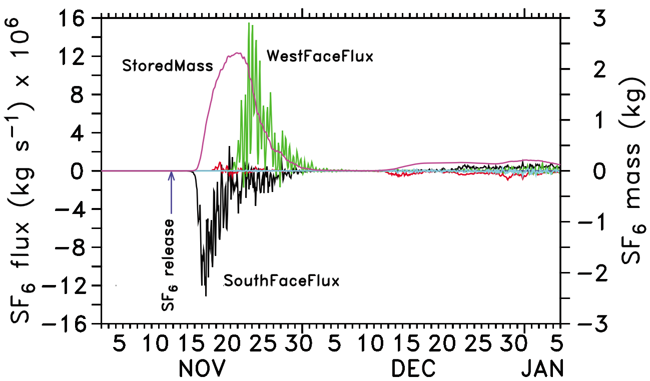

Figure 21. Mass flux of SF_6 (kg s^{-1}) through the faces of the large control volume (Figure 16), with positive flux directed outward. Fluxes through south and west faces are shown in black and green. Flux through the north, east, and top control surfaces are slight in comparison. Flux through the north face (red) is southward after 10 December. The total SF_6 within the large control volume, stored mass, at any instant (magenta) has a maximum value of 2.3 kg.

again northward, SF_6 had been transported too far west to be affected by flow through P1. The SF_6 by then was embedded in a flow that carried it farther westward, exclusive of some transport northward through the seamount passages.

5. Emerging Views of Abyssal Circulation and Transport at the EPR 9–10°N

[74] The combined observational and modeling results of the LADDER program show that regional flow and transport at the northern end of this EPR segment is complex and variable. The line segment topography of the ridge, the quasi-circular topography of the individual seamounts, and the quasi-ellipsoidal topography of the composite edifice of the seamount chain all combined with regional background flow having a preponderance of short- (tidal) and long-period (>200 h) spectral energy to create a wide variety of circulation and transport patterns. We summarize here the most important, recurrent large-scale physical oceanographic features that have emerged from this study, those that we believe will hold up under the scrutiny of more detailed measurements and more refined modeling.

[75] 1. Time-varying meridional jets are trapped to the ridge flank, a poleward jet to the west and an equatorward jet to the east of the ridge crest under typical background flow conditions. Jet distributions need not be antisymmetric across this ridge crest. In the case of background flow to the SSE, jets are present and meridional flow is still sheared across the ridge in the anticyclonic sense, but near flank flow on both sides of the ridge can be in the same direction. Jet velocities reaching as much as ~10 cm s^{-1} and jet cross-sectional widths reaching 10–20 km will vary with the strength and direction of the far-field flow. *McGillicuddy et al.* [2010] shows that inner edges of the jets sweep back and forth over the ridge crest, enhancing the low-frequency energy of meridional flow measured right above the EPR crest in comparison to the low-frequency energy of the corresponding zonal flow. These jets occur independently of hydrothermal heat flux. Jets are certain to be crucial in transporting material (e.g., larvae) between sites along the ridge.

[76] 2. Model hydrographic distributions are domed above the ridge crest and have isolines below the ridge crest that often plunge downward and into ridge flanks. Hydrographic distributions are typically asymmetric across the ridge crest. In many cases, isolines are lifted on the upstream and depressed on the downstream side of the ridge with respect to quasi-persistent cross-ridge flows. Down-ridge flank flows can relocate material originating on the crest to depths below the ridge and into the meridional jets as occurred with the SF_6 tracer. Plunging of isolines into the flanks of the ridge occurs independently of hydrothermal heating. Close spacing O(1–2 km) of hydrographic casts is likely needed to resolve the details of doming and below-ridge hydrographic asymmetries at abrupt ridge topography.

[77] 3. Passage P1 serves as a choke point for flow moving poleward along the western side of the 9–10°N ridge segment. During periods of west or WSW background flow, flow reaching P1 and the south side of seamount 1 in the jets typically will be split so that a fraction will continue north through P1 and the remainder will traverse westward on a trajectory south of the seamounts. The splitting fraction will depend on the background flow and its recent strength and directional history. In cases of SSE background flow, flow is southward through P1, blocking all poleward transport. During the 2006–2007 year of LADDER measurements, SSE regional flow prevailed >50% of the time. Westward transport along the south side of the seamounts is strongest during times of westward regional flow.

[78] 4. Passages between pairs of seamounts allow transport back and forth between the north and south sides of the Lamont seamount chain. During SSE background flow conditions, flow at the Lamont seamounts tends to be anticyclonic around the entire chain as a single edifice, anticyclonic around the three most western seamounts, and likely anticyclonic around the three eastern seamounts as well. Anticyclonic flow north of the seamounts promotes the return to the ridge of material that may have originally been advected west and then north around the end of the entire seamount chain or through the seamount passages. Model results suggest that this pathway was taken by some of the SF_6 in the actual tracer experiment. Model results also imply that the evolution of this particular SF_6 plume constitutes just one member from a wide range of possible outcomes for releases at the same site but at other times. Key factors that would determine outcomes are zonal flow at the time of release, the character of the along flank jets subsequent to release, the hydrodynamic conditions at passage P1 if and when the tracer arrives there, and the regional flow patterns thereafter.

[79] 5. Material advected to the northern tip of the ridge segment appears to have a high likelihood of being advected farther north into the abyssal ocean at the north end of the segment. Under westward zonal flow conditions, material reaching the westward end of the Lamont seamount chain is likely to be advected westward into the abyss as well.

[80] 6. The success in matching model and field observations to the degree they were matched depended on using a wide spectrum of frequencies in the model forcing having

amplitudes and phases, derived by inversion, that were reasonably comparable to those observed. Furthermore, the success depended on using the best source of information of abyssal motion during the simulation period and that was from currents measured on site. Interestingly, using spatially uniform barotropic forcing over this 200 km × 200 km domain proved to be an adequate assumption from which property distributions and flows developed. Had information on currents at the four corners of the domain been available, a different barotropic forcing description may have been possible. Over larger model domains and/or in regions where coherent structures like eddies are more prominent, the approach used here may be less successful.

Appendix A: Inverse Calculation

[81] Let currents over the ridge during the time period [0, T] that have been sampled N times at discrete intervals dt be represented in rotary spectral form [e.g., *Emery and Thomson*, 1998] by

$$(u+iv)_{ridge}^{measured} = A_n(\omega_n)\mathrm{e}^{i\omega_n t} + A_n'(\omega_n)\mathrm{e}^{-i\omega_n t}, \quad 0 < t < T, \tag{A1}$$

where summation over n on the right hand side is implied. Here u and v are the east and north components of current at time t, A_n and A_n' are complex coefficients at each frequency $\omega_n = 2\pi n/T$ for a set of frequencies determined by $n = \{0, 1, \ldots \mathrm{N}/2\}$, and $\mathrm{N} = \mathrm{T/dt}$.

[82] Analogous equations can be written for the first model input times series in the far field, the first model result at the ridge crest, and the second model input times series in the far field

$$(u+iv)_{farfield}^{model1\mathrm{st}} = B_n(\omega_n)\mathrm{e}^{i\omega_n t} + B_n'(\omega_n)\mathrm{e}^{-i\omega_n t}, \tag{A2}$$

$$(u+iv)_{ridge}^{model1\mathrm{st}} = C_n(\omega_n)\mathrm{e}^{i\omega_n t} + C_n'(\omega_n)\mathrm{e}^{-i\omega_n t}, \tag{A3}$$

$$(u+iv)_{farfield}^{model2\mathrm{nd}} = D_n(\omega_n)\mathrm{e}^{i\omega_n t} + D_n'(\omega_n)\mathrm{e}^{-i\omega_n t}. \tag{A4}$$

Suppose that a reasonable initial far-field time series (equation (A2)) can be estimated. Then that series can be used to derive $\vec{F}_B$ (equation (1)) and an initial model run can then be made. A time series of initial model results at CA (equation (A3)) can be recorded and that time series can be subsequently used to make a better estimate of the far-field current time series (equation (A4)).

[83] The coefficients D and D' of the new estimate are derived in this way. Suppose that the circulation model could be considered an operational transfer function of far-field current input to ridge current output and suppose that the transfer function were linear. Then the relationship of the time series at the ridge and in the far field could be written as

$$(u+iv)_{ridge}^{model1\mathrm{st}} = \int_0^T M(t-t')(u(t')+iv(t'))_{farfield}^{model1\mathrm{st}}\,dt', \tag{A5}$$

where M represents the model transform function. Replacing the two current time series in equation (A5) with their spectral representations (equations (A2) and (A4)) results in

$$C(\omega_n)e^{i\omega_n t} + C'(\omega_n)e^{-i\omega_n t} = \int_0^T M(t-t') \cdot \left(B(\omega_n)e^{i\omega_n t'} + B'(\omega_n)e^{-i\omega_n t'}\right)dt'. \tag{A6}$$

Similarly, if the second input far-field series could lead to a replication of actual currents on the ridge, that relationship would be written

$$A(\omega_n)e^{i\omega_n t} + A'(\omega_n)e^{-i\omega_n t} = \int_0^T M(t-t') \cdot \left(D(\omega_n)e^{i\omega_n t'} + D'(\omega_n)e^{-i\omega_n t'}\right)dt'. \tag{A7}$$

By the convolution theorem, equations (A6) and (A7) yield

$$C(\omega_n) = M(\omega_n)B(\omega_n), \tag{A8}$$

$$A(\omega_n) = M(\omega_n)D(\omega_n), \tag{A9}$$

with analogous equations for the primed variables A', B', C', and D'.

[84] Eliminating $M(\omega_n)$ from the equation pair (A8) and (A9) and the analogous primes variable equation pair results in

$$D(\omega_n) = (B(\omega_n)A(\omega_n))/C(\omega_n), \tag{A10}$$

$$D'(\omega_n) = (B'(\omega_n)A'(\omega_n))/C'(\omega_n). \tag{A11}$$

When these coefficients are reintroduced in equation (A4), a new estimate of $\vec{v}_{\mathrm{farfield}}$ results

$$(u+iv)_{farfield}^{model2\mathrm{nd}} = \left(\frac{BA}{C}\right)e^{i\omega_n t} + \left(\frac{B'A'}{C'}\right)e^{-i\omega_n t}. \quad 0 < t < T \tag{A12}$$

The circulation model is, in fact, not linear and the model results show strong along-ridge jets that are partly supported by the nonlinearity of the governing equations. On the other hand, at high frequencies, including tidal frequencies, an assumption of dynamical linearity is often made. Thus, for a substantial part of the frequency spectrum of our measurements equation (A12) should provide a better estimate than equation (A2) of the distant current time series to be used for forcing. Ultimately it is the correspondence of measured and modeled flow over the ridge crest summed over all frequencies that provides evidence of the utility of this primitive inverse approach.

[85] In practice, there is no need to stop at the second estimate of the distant currents, but a few pilot experiments we conducted suggested that the benefits of going to the

3rd estimate was not worth the computational cost. One additional practical matter in evaluating the coefficients of equation (A12) must be mentioned. Very small values of C and C' at some ω_n lead to unrealistically large spectral coefficients for the 2nd estimate, so that when $|A/C| > 1$ or $|A'/C'| > 1$, the ratio was reset to one. The reason is that amplitude in the distant region must be expected to be equal to or less than the amplitude above the topography at each ω_n.

[86] A similar strategy was used to construct the distal forcing current time series for 2-D model experiments reported by *McGillicuddy et al.* [2010]. In the present case, however, B and B' amplitudes were taken to be the amplitudes from the currents measured at the ridge divided by two after first removing a 10 day boxcar mean time series from the CA meridional current data. The reason for the last was that spectra at EF and WF showed considerably less low-frequency energy than did CA and the $\vec{v}_{\mathrm{farfield}}$ spectra is more likely to qualitatively resemble the spectra at EF and WF than at CA.

[87] **Acknowledgments.** The work of the lead author was funded by NOAA's Pacific Marine Environmental Laboratory and by NOAA's Vents Program. The work of the other authors has been supported by the Biological and Physical Oceanography Sections of the Division of Ocean Sciences of the NSF under grants OCE-0424953 and OCE-0425361, Larval Dispersion along the Deep East Pacific Rise (LADDER). This is contribution 3537 from NOAA's Pacific Marine Environmental Laboratory. The freeware application Ferret was used to analyze and display data sets.

References

Adams, D. K. (2007), Influence of hydrodynamics on the larval supply to hydrothermal vents on the East Pacific Rise, Ph.D. thesis, Mass. Inst. of Technol., Cambridge, Mass.

Adams, D. K., and G. R. Flierl (2010), Modeled interactions of mesoscale eddies with the East Pacific Rise: Implications for larval dispersal, *Deep Sea Res. Part I*, *57*, 1163–1176.

Adams, D. K., and L. S. Mullineaux (2008), Supply of gastropod larvae to hydrothermal vents reflects transport from local larval sources, *Limnol. Oceanogr.*, *53*, 1945–1955.

Baker, E. T., R. A. Feely, M. J. Mottl, F. T. Sansone, C. G. Wheat, J. A. Resing, and J. E. Lupton (1994), Hydrothermal plumes along the East Pacific Rise, 8°40′N to 11°50′N: Plume distribution and relationship to the apparent magmatic budget, *Earth Planet. Sci. Lett.*, *128*, 1–17, doi:10.1016/0012-821X(94)90022-1.

Berdeal, I. G., S. L. Hautala, L. N. Thomas, and H. P. Johnson (2006), Vertical structure of time-dependent currents in a mid-ocean ridge axial valley, *Deep Sea Res. Part I*, *53*, 367–386, doi:10.1016/j.dsr.2005.10.004.

Brink, K. H. (1995), Tidal and lower frequency currents above Fieberling Guyot, *J. Geophys. Res.*, *100*, 10,817–10,832, doi:10.1029/95JC00998.

Cannon, G. A., and D. J. Pashinski (1997), Variations in mean currents affecting hydrothermal plumes on the Juan de Fuca Ridge, *J. Geophys. Res.*, *102*, 24,965–24,976, doi:10.1029/97JC01910.

Cannon, G. A., D. J. Pashinski, and M. R. Lemon (1991), Middepth flow near hydrothermal venting sites on the southern Juan de Fuca Ridge, *J. Geophys. Res.*, *96*, 12,815–12,831, doi:10.1029/91JC01023.

Cannon, G. A., D. J. Pashinski, and T. J. Stanley (1995), Fate of event hydrothermal plumes on the Juan de Fuca Ridge, *Geophys. Res. Lett.*, *22*, 163–166, doi:10.1029/94GL02280.

Chevaldonné, P., D. Jollivet, A. Vangriesheim, and D. Desbruyeres (1997), Hydrothermal-vent alvinellid polychaete dispersal in the eastern Pacific, part 1. Influence of vent site distribution, bottom currents, and biological patterns, *Limnol. Oceanogr.*, *42*, 67–80, doi:10.4319/lo.1997.42.1.0067.

Crane, K., F. Aikman, R. W. Embley, S. R. Hammond, A. Malahoff, and J. Lupton (1985), The distribution of geothermal fields on the Juan de Fuca Ridge, *J. Geophys. Res.*, *90*, 727–744, doi:10.1029/JB090iB01p00727.

Doherty, K. W., D. E. Frye, S. P. Liberatore, and J. M. Toole (1999), A moored profiling instrument, *J. Atmos. Oceanic Technol.*, *16*, 1816–1829, doi:10.1175/1520-0426(1999)016<1816:AMPI>2.0.CO;2.

Emery, W. J., and R. E. Thomson (1998), *Data Analysis Methods in Physical Oceanography*, Pergamon, New York.

Fiedler, P. C., and L. D. Talley (2006), Hydrography of the eastern tropical Pacific: A review, *Prog. Oceanogr.*, *69*, 143–180, doi:10.1016/j.pocean.2006.03.008.

Fornari, D. J., M. R. Perfit, J. F. Allan, R. Batiza, R. Haymon, A. Barone, W. B. F. Ryan, T. Smith, T. Simkin, and M. A. Luckman (1988), Geochemical and structural studies of the Lamont seamount—Seamounts as indicators of mantle processes, *Earth Planet. Sci. Lett.*, *89*, 63–83, doi:10.1016/0012-821X(88)90033-7.

Fornari, D. J., R. M. Haymon, M. R. Perfit, and M. H. Edwards (1998), Axial summit trough of the East Pacific Rise 9°–10°N: Geological characteristics and evolution of the axial zone on fast spreading mid-ocean ridges, *J. Geophys. Res.*, *103*, 9827–9855, doi:10.1029/98JB00028.

Haymon, R. M., D. J. Fornari, M. H. Edwards, S. Carbotte, D. Wright, and K. C. Macdonald (1991), Hydrothermal vent distribution along the East Pacific Rise crest (9°09′–54′N) and its relationship to magmatic and tectonic processes on fast-spreading midocean ridges, *Earth Planet. Sci. Lett.*, *104*, 513–534, doi:10.1016/0012-821X(91)90226-8.

Helfrich, K. R., T. M. Joyce, G. A. Cannon, S. A. Harrington, and D. J. Pashinski (1998), Mean hydrographic and velocity sections near Pipe Organ vent at Juan de Fuca Ridge, *Geophys. Res. Lett.*, *25*, 1737–1740, doi:10.1029/98GL01308.

Holloway, P. E., and M. A. Merrifield (1999), Internal tide generation by seamounts, ridges, and islands, *J. Geophys. Res.*, *104*, 25,937–25,951, doi:10.1029/1999JC900207.

Jackson, P. R., J. R. Ledwell, and A. M. Thurnherr (2010), Dispersion of a tracer on the East Pacific Rise (9°N to 10°N), including the influence of hydrothermal plumes, *Deep Sea Res. Part I*, *57*, 37–52, doi:10.1016/j.dsr.2009.10.011.

Joyce, T. M. (1981), The influence of the mid Atlantic Ridge upon the circulation and the properties of the Mediterranean Water southwest of the Azores, *J. Mar. Res.*, *39*, 31–52.

Joyce, T. M., G. A. Cannon, D. Pashinski, K. R. Helfrich, and S. A. Harrington (1998), Vertical and temporal vorticity observations at Juan de Fuca Ridge: Hydrothermal signatures, *Geophys. Res. Lett.*, *25*, 1741–1744, doi:10.1029/98GL01309.

Keller, G. H., S. H. Anderson, and J. W. Lavelle (1975), Near-bottom currents in mid-Atlantic ridge rift valley, *Can. J. Earth Sci.*, *12*, 703–710.

Lavelle, J. W. (1997), Buoyancy-driven plumes in rotating, stratified cross flows: Plume dependence on rotation, turbulent mixing, and cross-flow strength, *J. Geophys. Res.*, *102*, 3405–3420, doi:10.1029/96JC03601.

Lavelle, J. W. (2006), Flow, hydrography, turbulent mixing, and dissipation at Fieberling Guyot examined with a primitive equation model, *J. Geophys. Res.*, *111*, C07014, doi:10.1029/2005JC003224.

Lavelle, J. W., and W. C. Thacker (2008), A pretty good sponge: Dealing with open boundaries in limited-area ocean models, *Ocean Modell.*, *20*, 270–292, doi:10.1016/j.ocemod.2007.10.002.

Mahadevan, A. (2006), Modeling vertical motion at ocean fronts: Are non-hydrostatic effects relevant at submesoscales?, *Ocean Modell.*, *14*, 222–240, doi:10.1016/j.ocemod.2006.05.005.

Marsh, A. G., L. S. Mullineaux, C. M. Young, and D. T. Manahan (2001), Larval dispersal potential of the tubeworm *Riftia pachyptila* at deep-sea hydrothermal vents, *Nature*, *411*, 77–80, doi:10.1038/35075063.

McGillicuddy, D. J., J. W. Lavelle, A. M. Thurnherr, V. K. Kosnyrev, and L. S. Mullineaux (2010), Larval dispersion along an axially symmetric mid-ocean ridge, *Deep Sea Res. Part I*, *57*, 880–892, doi:10.1016/j.dsr.2010.04.003.

Mullineaux, L. S., D. K. Adams, S. W. Mills, and S. E. Beaulieu (2010), Larvae from afar colonize deep-sea hydrothermal vents after a catastrophic eruption, *Proc. Natl. Acad. Sci. U. S. A.*, *107*, 7829–7834, doi:10.1073/pnas.0913187107.

Roden, G. I. (1987), Effects of seamounts and seamount chains on ocean circulation and thermohaline structure, in *Seamounts, Islands and Atolls*, *Geophys. Monogr. Ser.*, vol. 43, edited by B. Keating et al., pp. 335–354, AGU, Washington, D. C.

Smagorinsky, J. (1993), Some historical remarks on the use of nonlinear viscosities, in *Large Eddy Simulation of Complex Engineering and Geophysical Flows*, edited by B. Galperin and S. A. I. Orsag, pp. 3–36, Cambridge Univ. Press, New York.

Smolarkiewicz, P. K., and L. G. Margolin (1998), MPDATA: A finite-difference solver for geophysical flows, *J. Comput. Phys.*, *140*, 459–480, doi:10.1006/jcph.1998.5901.

Stommel, H., E. D. Stroup, J. L. Reid, and B. A. Warren (1973), Transpacific hydrographic sections at Latitudes 43°S and 28°S: The Scorpio Expedition—Part I. Preface, *Deep Sea Res. Oceanogr. Abstracts*, *20*, 1–7.

Thompson, L., and G. C. Johnson (1996), Abyssal currents generated by diffusion and geothermal heating over rises, *Deep Sea Res. Part I*, *43*, 193–211, doi:10.1016/0967-0637(96)00095-7.

Thomson, R. E., S. F. Mihaly, A. B. Rabinovich, R. E. McDuff, S. R. Veirs, and F. R. Stahr (2003), Constrained circulation at Endeavour ridge facilitates colonization by vent larvae, *Nature*, *424*, 545–549, doi:10.1038/nature01824.

Thomson, R. E., M. M. Subbotina, and M. V. Anisimov (2009), Numerical simulation of mean currents and water property anomalies at Endeavour Ridge: Hydrothermal versus topographic forcing, *J. Geophys. Res.*, *114*, C09020, doi:10.1029/2008JC005249.

Thurnherr, A. M., G. Reverdin, P. Bouruet-Aubertot, L. C. St. Laurent, A. Vangriesheim, and V. Ballu (2008), Hydrography and flow in the Lucky Strike segment of the Mid-Atlantic Ridge, *J. Mar. Res.*, *66*, 347–372, doi:10.1357/002224008786176034.

Wunsch, C., D. X. Hu, and B. Grant (1983), Mass, heat, salt and nutrient fluxes in the South Pacific Ocean, *J. Phys. Oceanogr.*, *13*, 725–753, doi:10.1175/1520-0485(1983)013<0725:MHSANF>2.0.CO;2.

Zaron, E. D., and G. D. Egbert (2006), Verification studies for a z-coordinate primitive-equation model: Tidal conversion at a mid-ocean ridge, *Ocean Modell.*, *14*, 257–278, doi:10.1016/j.ocemod.2006.05.007.

J. W. Lavelle, NOAA Pacific Marine Environmental Laboratory, 7600 Sand Point Way NE, Seattle, WA 98115, USA. (j.williams.lavelle@noaa.gov)

J. R. Ledwell and D. J. McGillicuddy Jr., Department of Applied Ocean Physics and Engineering, Woods Hole Oceanographic Institution, Woods Hole, MA 02543, USA.

L. S. Mullineaux, Department of Biology, Woods Hole Oceanographic Institution, Woods Hole, MA 02543, USA.

A. M. Thurnherr, Division of Ocean and Climate Physics, Lamont-Doherty Earth Observatory, PO Box 1000, Palisades, NY 10964-1000, USA.